

## THE CHEMICAL ABUNDANCES OF STARS IN THE HALO (CASH) PROJECT. II. A SAMPLE OF 14 EXTREMELY METAL-POOR STARS<sup>\*,†</sup>

JULIE K. HOLLEK<sup>1</sup>, ANNA FREBEL<sup>2</sup>, IAN U. ROEDERER<sup>3</sup>, CHRISTOPHER SNEDEN<sup>1</sup>, MATTHEW SHETRONE<sup>1,4</sup>,

TIMOTHY C. BEERS<sup>5</sup>, SUNG-JU KANG<sup>6</sup>, AND CHRISTOPHER THOM<sup>7</sup>

<sup>1</sup> Department of Astronomy, University of Texas at Austin, Austin, TX 78712, USA;

[julie@astro.as.utexas.edu](mailto:julie@astro.as.utexas.edu), [chris@astro.as.utexas.edu](mailto:chris@astro.as.utexas.edu), [shetrone@astro.as.utexas.edu](mailto:shetrone@astro.as.utexas.edu)

<sup>2</sup> Harvard-Smithsonian Center for Astrophysics, Cambridge, MA 02138, USA; [afrebel@cfa.harvard.edu](mailto:afrebel@cfa.harvard.edu)

<sup>3</sup> Carnegie Observatories, Pasadena, CA 91101, USA; [iur@obs.carnegiescience.edu](mailto:iur@obs.carnegiescience.edu)

<sup>4</sup> McDonald Observatory, University of Texas, Fort Davis, TX 78734, USA

<sup>5</sup> Department of Physics and Astronomy, and JINA: Joint Institute for Nuclear Astrophysics,

Michigan State University, East Lansing, MI 48824, USA; [beers@pa.msu.edu](mailto:beers@pa.msu.edu)

<sup>6</sup> Department of Physics and Astronomy, Iowa State University, Ames, IA 50011, USA; [sjkang@iastate.edu](mailto:sjkang@iastate.edu)

<sup>7</sup> Space Telescope Science Institute, Baltimore, MD 21218, USA; [cthom@stsci.edu](mailto:cthom@stsci.edu)

Received 2011 June 15; accepted 2011 August 11; published 2011 November 3

### ABSTRACT

We present a comprehensive abundance analysis of 20 elements for 16 new low-metallicity stars from the Chemical Abundances of Stars in the Halo (CASH) project. The abundances have been derived from both Hobby-Eberly Telescope High Resolution Spectrograph snapshot spectra ( $R \sim 15,000$ ) and corresponding high-resolution ( $R \sim 35,000$ ) Magellan Inamori Kyocera Echelle spectra. The stars span a metallicity range from  $[\text{Fe}/\text{H}]$  from  $-2.9$  to  $-3.9$ , including four new stars with  $[\text{Fe}/\text{H}] < -3.7$ . We find four stars to be carbon-enhanced metal-poor (CEMP) stars, confirming the trend of increasing  $[\text{C}/\text{Fe}]$  abundance ratios with decreasing metallicity. Two of these objects can be classified as CEMP-no stars, adding to the growing number of these objects at  $[\text{Fe}/\text{H}] < -3$ . We also find four neutron-capture-enhanced stars in the sample, one of which has  $[\text{Eu}/\text{Fe}]$  of 0.8 with clear  $r$ -process signatures. These pilot sample stars are the most metal-poor ( $[\text{Fe}/\text{H}] \lesssim -3.0$ ) of the brightest stars included in CASH and are used to calibrate a newly developed, automated stellar parameter and abundance determination pipeline. This code will be used for the entire  $\sim 500$  star CASH snapshot sample. We find that the pipeline results are statistically identical for snapshot spectra when compared to a traditional, manual analysis from a high-resolution spectrum.

*Key words:* Galaxy: halo – methods: data analysis – stars: abundances – stars: atmospheres – stars: Population II

*Online-only material:* color figures, machine-readable tables

### 1. INTRODUCTION

The first stars formed from metal-free material in the early universe and therefore are thought to have been massive ( $\sim 100 M_{\odot}$ ; e.g., Bromm et al. 1999). Many of these first stars polluted the surrounding local environment with their chemical feedback through core-collapse supernovae. From this enriched material, subsequent generations of stars were born. Due to the presence of additional cooling mechanisms, these stars had a range of lower masses and thus were longer lived (e.g., Bromm & Loeb 2003).

Today, we observe the surviving low-mass stars as the most metal-poor stars in the Galaxy. The atmospheres of these objects contain the chemical signatures of early supernova events. By studying these stars, constraints can be placed on the specific types of nucleosynthetic events responsible for the observed abundance patterns.

Efforts to classify metal-poor stars have been based upon metallicity,  $[\text{Fe}/\text{H}]$ ,<sup>8</sup> and chemical composition,  $[\text{X}/\text{Fe}]$ , to better understand the diversity of the observed abundance

patterns (Beers & Christlieb 2005). Stars with  $[\text{Fe}/\text{H}] < -3.0$  are labeled as extremely metal-poor (EMP). The metallicity distribution function shows that as metallicity decreases, the number of stars in each metallicity bin rapidly decreases (Ryan & Norris 1991; Carney et al. 1996; Schörck et al. 2009; Li et al. 2010). Only  $\sim 25$  of these EMP stars have  $[\text{Fe}/\text{H}] \lesssim -3.5$ . Below  $[\text{Fe}/\text{H}] \sim -3.6$  there is a sharp drop in the number of stars, so extreme EMPs are an important probe of this tail. To date, only three stars with  $[\text{Fe}/\text{H}] < -4.5$  have been discovered, with two considered to be hyper metal-poor ( $[\text{Fe}/\text{H}] < -5.0$ ; Christlieb et al. 2004; Frebel et al. 2005; Norris et al. 2007).

The majority of metal-poor stars ( $[\text{Fe}/\text{H}] < -1$ ) show abundance patterns similar to the solar system, but scaled down by metallicity, with two main differences: there is an enhancement in the  $\alpha$ -elements (e.g.,  $[\text{Mg}/\text{Fe}]$ ) and a depletion in some of the Fe-peak elements (e.g.,  $[\text{Mn}/\text{Fe}]$ ) compared to the solar abundance ratios. This pattern can be explained with enrichment by previous core-collapse supernovae (e.g., Heger & Woosley 2010). The chemical outliers among stars with  $[\text{Fe}/\text{H}] < -2.0$ , which make up perhaps 10%, show great diversity in their abundance patterns. Many stars have overabundances in selected groups of elements, e.g., the rapid ( $r$ ) neutron-capture process elements (Sneden et al. 2008) and/or the slow ( $s$ ) neutron-capture process elements. The frequency of chemically unusual stars increases with decreasing metallicity, with stars often belonging to multiple chemical outlier groups. Not included in this estimate of chemically unusual stars are the so-called carbon-enhanced

<sup>\*</sup> Based on observations obtained with the Hobby-Eberly Telescope, which is a joint project of the University of Texas at Austin, the Pennsylvania State University, Stanford University, Ludwig-Maximilians-Universität München, and Georg-August-Universität Göttingen.

<sup>†</sup> Based on observations gathered with the 6.5 m Magellan Telescopes located at Las Campanas Observatory, Chile.

<sup>8</sup>  $[\text{A}/\text{B}] \equiv \log(N_{\text{A}}/N_{\text{B}}) - \log(N_{\text{A}}/N_{\text{B}})_{\odot}$  for N atoms of elements A, B, e.g.,  $[\text{Fe}/\text{H}] = -3.0$  is 1/1000 of the solar Fe abundance.

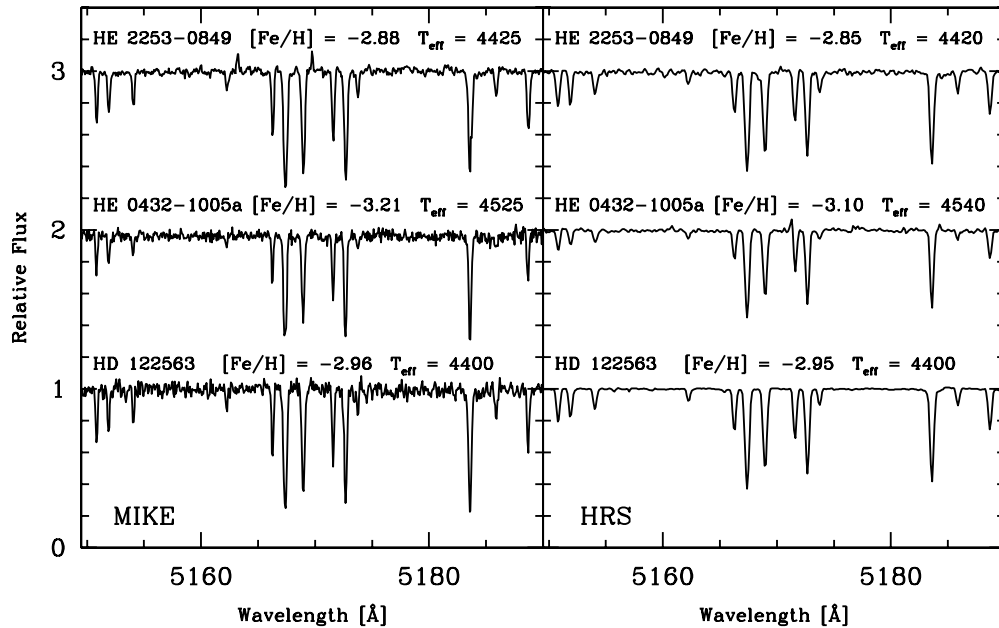


**Figure 1.** MIKE (left) and HRS (right) spectra of three stars with derived spectroscopic  $T_{\text{eff}} \sim 4500$  K. Both HRS and MIKE derived  $[\text{Fe}/\text{H}]$  values are listed for each star.

metal-poor (CEMP) stars (where  $[\text{C}/\text{Fe}] > 0.7$ ), which make up at least  $\sim 15\%$  of stars with  $[\text{Fe}/\text{H}] < -2.0$ . At the lowest metallicities, the frequency of CEMP stars also increases (Beers & Christlieb 2005; Lucatello et al. 2006; Frebel et al. 2006; Cohen et al. 2006; Carollo et al. 2011). In fact, all three  $[\text{Fe}/\text{H}] < -4.5$  stars are CEMP stars.

Medium-resolution spectra ( $R \sim 2000$ ) can be used to determine the overall metallicity based upon the strength of the  $\text{Ca II K}$  line. However, medium-resolution spectra provide limited information on the abundances of individual elements, especially at low metallicity. High-resolution (e.g.,  $R \sim 40,000$ ) observations are necessary to carry out detailed analyses which yield abundances with small uncertainties ( $\sim 0.1$  dex). These observations are, however, more time-consuming and require large telescopes to achieve an adequate signal-to-noise ratio (S/N) in the data.

“Snapshot” spectra, with intermediate resolution ( $R \sim 15,000$ – $20,000$ ) and moderate S/N ( $\sim 40$ ), fill the gap between time intensive high- and medium-resolution observations. From such snapshot data, abundances for  $\sim 15$  elements can be derived with moderate uncertainties ( $\sim 0.25$  dex; Barklem et al. 2005). This allows for a more efficient confirmation of EMP stars and chemical outliers. The Barklem et al. (2005), Hamburg/ESO R-process Enhanced Star (hereafter HERES) study itself determined abundances (and upper limits) for a total of  $\sim 250$  stars based on Very Large Telescope (VLT)/UVES snapshot spectra.

The Chemical Abundances of Stars in the Halo (CASH) project is a dedicated effort that aims to provide abundances for  $\sim 500$  metal-poor stars primarily based on  $R \sim 15,000$ , moderate-S/N snapshot spectra taken with the High Resolution Spectrograph (HRS; Tull 1998) on the fully queue scheduled (Shetrone et al. 2007) Hobby-Eberly Telescope (HET). One of the earliest results of the CASH project was the discovery of an unusual, Li-enhanced giant HKII 17435–00532 (Roederer et al. 2008). Given the large number of stars in the sample, it is expected that there will be additional chemically unusual stars.

In this paper, we study the CASH pilot sample of 16 stars, spanning a metallicity range of  $\sim 1.0$  dex, from  $[\text{Fe}/\text{H}] \sim -2.9$  to  $-3.9$ . The aim of the present study is twofold: to present

abundance analyses for the 16 most metal-poor stars included in the CASH project and to use those abundances to calibrate the newly developed stellar parameter and abundance pipeline. We will use it to obtain abundances for the full  $\sim 500$  star CASH sample (J. K. Hollek et al. 2012, in preparation).

In Section 2, we discuss the spectra in terms of the sample selection, observational information, and data reduction. In Section 3, we introduce our spectral analysis tools, including our line list, equivalent width measurement routines, and model atmosphere analysis code. In Sections 4 and 5, we describe acquisition of our stellar parameters for both sets of data and a comparison between the two. In Section 6, we discuss the abundance analysis methods for each element we measure, including the error analysis and comparison of our results to those in the literature. Section 7 includes a summary of our abundance results and discussion of the implications of our derived abundances. In Section 8, we list our summary.

## 2. OBSERVATIONS

### 2.1. Sample Selection

The stars of the pilot study were chosen from the Hamburg/ESO Bright Metal-Poor Sample (BMPS; Frebel et al. 2006) of the Hamburg/ESO objective-prism plate Survey (HES; Christlieb et al. 2001). These stars ( $B < 14.5$ ) required extra processing due to saturation of the photographic plates. Around 170 new metal-poor stars with  $[\text{Fe}/\text{H}] < -2.0$  were identified from medium-resolution spectra; most of the BMPS stars observable from McDonald Observatory were added to the CASH sample in order to obtain snapshot spectra with the HET. This paper includes 16 HES BMPS objects, chosen as the most metal-poor HES BMPS stars in the CASH study. We also included five new high-resolution observations of well-studied stars from the literature for comparison purposes. All 16 HES objects have high-resolution observations. Of these objects, 14 have HRS spectra. Only one standard star, HD 122563, has an HRS spectrum. Figure 1 shows both the HRS and Magellan Inamori Kyocera Echelle (MIKE) spectra of three representative stars in this sample. The full  $\sim 500$  star sample contains targets

**Table 1**  
Observations

Star	Telescope	UT Date	R.A. (J2000)	Decl. (J2000)	$t_{\text{exp}}$ (s)	S/N (at 5180 Å)	$v_{\text{rad}}$ (km s <sup>-1</sup> )
HE 0013–0257	HET	2007 Jul 28	00 16 04.2	–02 41 06	630	65	47.7
	Magellan	2006 Sep 28			600	34	45.4
HE 0013–0522	HET	2007 Aug 8	00 16 28.1	–05 05 52	678	85	–174.7
	Magellan	2010 Aug 8			1800	81	–175.5
HE 0015 + 0048	HET	2007 Aug 10	00 18 01.4	+01 05 08	888	70	–40.8
	Magellan	2010 Aug 8			1800	56	–48.8
HE 0302–3417a	Magellan	2006 Sep 27	03 04 28.6	–34 06 06	300	88	121.7
HE 0324 + 0152a	HET	2008 Feb 24	03 26 53.8	+02 02 28	316	65	107.3
	Magellan	2006 Sep 27			450	70	106.1
HE 0420 + 0123a	HET	2008 Jan 5	04 23 14.4	+01 30 49	207	180 <sup>a</sup>	–53.3
	HET	2009 Nov 12			800	...	–52.8
HE 0432–1005a	Magellan	2006 Sep 28	04 35 01.2	–09 59 36	300	64	–55.3
	HET	2008 Nov 10			890	80 <sup>a</sup>	198.0
	HET	2009 Nov 12			1800	...	199.6
HE 1116–0634	Magellan	2006 Sep 28	11 18 35.8	–06 50 46	900	44	197.3
	HET	contaminated <sup>b</sup>			...	...	...
HE 1311–0131	Magellan	2010 Jul 3	13 13 42.0	–01 47 16	1200	121	115.5
	HET	2008 Apr 6			250	45	125.8
HE 1317–0407	Magellan	2010 Aug 5	13 19 47.0	–04 23 10	2736	48	124.7
	HET	contaminated <sup>b</sup>			...	...	...
HE 2123–0329	Magellan	2010 Jul 3	21 26 08.9	–03 16 58	487	135	124.7
	HET	2008 Jun 28			1473	65	–218.8
HE 2138–0314	Magellan	2010 Aug 5	21 40 41.5	–03 01 17	1800	85	–219.4
	HET	2009 Nov 13			600	85 <sup>a</sup>	–371.0
	HET	2008 Jul 14			891	...	–371.6
HE 2148–1105a	Magellan	2010 Aug 5	21 50 41.5	–10 50 58	1304	93	–373.5
	HET	contaminated <sup>b</sup>			...	...	...
HE 2238–0131	Magellan	2010 Aug 6	22 40 38.1	–01 16 16	300	61	–87.17
	HET	2008 Nov 13			494	60	–185.0
HE 2253–0849	Magellan	2010 Aug 8	22 55 43.1	–08 33 28	1200	96	–186.7
	HET	2008 Nov 13			427	75	–89.4
HE 2302–2154a	Magellan	2010 Aug 8	23 05 25.2	–21 38 07	1200	63	–91.1
	HET	2006 Sep 28			450	55	–17.8
HD 122563	HET	2009 Mar 1	14 02 31.8	+09 41 10	30	300	–25.4
	Magellan	2009 Jul 26			5	35	–25.7
CD –38 245	Magellan	2009 Jul 27	00 46 36.2	–37 39 33	250	65	47.1
CS 22891–200	Magellan	2010 Aug 5	20 19 22.0	–61 30 15	900	52	137.7
CS 22873–166	Magellan	2009 Jul 27	19 35 19.1	–61 42 24	120	53	–16.2
BD –18 5550	Magellan	2009 Jul 27	19 58 49.7	–18 12 11	87	157	–125.3

**Notes.**<sup>a</sup> S/N for combined HET spectra.<sup>b</sup> Sky contamination in spectrum, excluded from this analysis.

from other surveys including the Sloan Digital Sky Survey (York et al. 2000), the Sloan Extension for Galactic Understanding and Exploration (Yanny et al. 2009), and the HK (Beers et al. 1985, 1992) surveys.

Of the HRS snapshot spectra included in this study, three spectra were substantially contaminated with the solar spectrum, with no available sky fibers to properly correct the data. From these spectra, we were able to determine that the [Fe/H] values for the stars were roughly  $-3.0$ ; however, these spectra require further processing in order to derive accurate stellar parameters and abundances. The snapshot-derived results for these stars will be included in a future paper, though we present the abundances derived from the high-resolution MIKE spectra here.

## 2.2. Spectroscopy

The snapshot spectra for the CASH project were obtained using the fiber-fed HRS on the HET at McDonald Observatory. The CASH spectra were obtained with a 2'' fiber yielding

$R \sim 15,000$ . The  $2 \times 5$  on-chip CCD binning leads to 3.2 pixels per resolution element. Two CCDs were used to record the red and blue portions of the spectrum. The useful wavelength range is from 4200–7800 Å, or from the CH *G*-band to the oxygen triplet. The median S/N value for the entire 500 star sample is  $\sim 65$ , with a median S/N value for the pilot sample of 70; see Table 1. There is substantially lower S/N at the blue ends of the spectra, given the combination of the somewhat poor blue response of the HRS and the lack of blue flux for many of the objects observed in CASH, especially the cool giants.

High-resolution spectra for 21 stars were obtained using the MIKE instrument (Bernstein et al. 2003) on the Magellan-Clay Telescope at Las Campanas Observatory. We used the 0'.7 slit with  $2 \times 2$  on-chip binning, yielding a nominal resolution of  $R \sim 35,000$  in the blue and 28,000 in the red with average S/N  $\sim 85$  at 5200 Å. MIKE spectra have nearly full optical wavelength coverage from  $\sim 3500$ –9000 Å.

Table 1 lists the details of the observations for each star on both telescopes.

### 2.3. Data Reduction

The HRS spectra were reduced using the IDL pipeline REDUCE (Piskunov & Valenti 2002), which performs standard echelle reduction techniques (trimming, bias subtraction, flat fielding, order tracing, and extraction). The data were wavelength calibrated using ThAr lamp exposures taken before or after every observation. Comparisons have been made between a by-hand IRAF<sup>9</sup> reduction and the REDUCE reduction of medium-S/N HRS data. Both yield comparable S/N across the spectrum, and the measured equivalent widths for 121 different lines differ between the two different reductions by  $3 \pm 8 \text{ m}\text{\AA}$ , which is statistically insignificant (Roederer et al. 2008). In addition, earlier tests of REDUCE versus IRAF have shown that the optimized extraction in REDUCE for high S/N spectra yields an extracted spectrum that is less noisy than that of a spectrum extracted in IRAF (see Figure 8 in Piskunov & Valenti 2002). Standard IRAF routines were then used to coadd (in the case of multiple observations) and continuum normalize the individual observations into a final one-dimensional (1D) spectrum. Radial velocities were computed by cross-correlating the echelle order containing the Mg b triplet against another metal-poor giant observed with the same instrumental setup. Typical uncertainties were  $2\text{--}3 \text{ km s}^{-1}$  for a single observation. Barycentric velocity corrections were computed using the IRAF “rvcorrect” routine.

Spectra observed using the MIKE instrument were reduced using an echelle data reduction pipeline made for MIKE<sup>10</sup> and then normalized and coadded using the same method as the HRS spectra.

## 3. SPECTRAL ANALYSIS

### 3.1. Line List

The line list to analyze the HRS spectra was based on the lines included in Roederer et al. (2010). Only those lines which are unblended at the median S/N and resolution of the typical HRS snapshot spectrum were included in our final list.

The line list for the MIKE data is a composite of the lines from Roederer et al. (2010), supplemented with additional lines from Cayrel et al. (2004) and Aoki et al. (2007b). This line list includes lines used for the HRS snapshot spectra analysis. Where the same line was included in more than one line list, the most up-to-date oscillator strength was used, following Roederer et al. (2010). We confirmed that all important lines for our abundance analysis were included in this line list by plotting the position of each line against a high-resolution MIKE spectrum of a star with a higher metallicity than that of any star in the pilot sample. Compared to the sample stars, this star displays many more absorption lines. This also allowed us to visually inspect for features that were not present in both an EMP star and a star that is still considered to be metal-poor, but with substantially higher (1 dex) [Fe/H].

### 3.2. Line Measurements

In each spectrum, we measured equivalent widths of unblended lines of various elements. Table 2 lists the element

**Table 2**  
Equivalent Widths

Star	Ion	Wavelength ( $\text{\AA}$ )	XP	log gf	EW (m $\text{\AA}$ )
HE 0015+0048	12.0	3986.75	4.35	−1.030	27.5
HE 0015+0048	12.0	4057.50	4.35	−0.890	41.9
HE 0015+0048	12.0	4167.27	4.35	−0.710	64.9
HE 0015+0048	12.0	4571.09	0.00	−5.688	57.7
HE 0015+0048	12.0	4702.99	4.33	−0.380	65.1
HE 0015+0048	12.0	5528.40	4.34	−0.498	78.2
HE 0015+0048	13.0	3961.52	0.01	−0.340	125.1
HE 0015+0048	20.0	4226.73	0.00	0.244	210.3
HE 0015+0048	20.0	4289.36	1.88	−0.300	51.7
HE 0015+0048	20.0	4318.65	1.89	−0.210	42.5
...					

**Notes.** We list the ionization state of each element where .0 indicates a neutral species and .1 indicates a singly ionized species.

(This table is available in its entirety in a machine-readable form in the online journal. A portion is shown here for guidance regarding its form and content.)

and ionization state, equivalent widths, wavelength, excitation potential, and oscillator strengths of each measured line in the MIKE spectra. These equivalent widths were used to determine stellar parameters and abundances for  $\sim 10$  elements. The equivalent widths in the HRS spectra were measured using an IDL routine. Here we briefly summarize the features important to this work. The routine works to automatically fit a Voigt profile to each line. The user can then manually adjust the continuum level, the number of spectral points over which the line is fit, and the line center, among other features. Given the limitations of resolution and S/N, some lines used in the analysis for HRS spectra depart from the linear portion of the curve of growth; thus, line fits using the Voigt profile, rather than simply a Gaussian fit, are preferred.

The equivalent widths in the high-resolution spectra were measured with an ESO/Midas routine, which automatically fits Gaussian profiles to each line. The user can calculate a fit to the continuum level by selecting line-free continuum regions. This code takes into account any possible non-zero slope of the continuum.

We chose a different equivalent width measurement routine because the higher S/N of the MIKE spectra allowed us to detect deviations from zero in the slope of the continuum that may arise from small-scale variation in imperfectly normalized spectra or nearby strong lines. Thus, it was helpful to be able to make a linear fit when determining the continuum. Additionally, the larger wavelength range allowed for more lines to be measured, thereby enabling us to exclude lines near the flat part of the curve of growth. Table 2 lists the equivalent widths for all of our stars in the pilot sample.

Figure 2 shows our measured equivalent widths from the MIKE spectrum of BD −18 5550 plotted against the equivalent widths measured for the same star by Cayrel et al. (2004). We find a mean difference of  $-0.6 \text{ m}\text{\AA}$  with  $\sigma = 2.4 \text{ m}\text{\AA}$  between the MIKE and Cayrel et al. (2004) measurements for lines included in our analysis. We also made a comparison between the equivalent widths measured from the HRS and MIKE spectra for a representative star, as we did not have an HRS spectrum for BD −18 5550 because it is not observable from McDonald Observatory. We find a mean difference of  $2.5 \text{ m}\text{\AA}$  with  $\sigma = 3.4 \text{ m}\text{\AA}$ . In both comparisons, between the MIKE spectra measured equivalent widths and those of the Cayrel et al. (2004) study as well as between the MIKE spectra and the

<sup>9</sup> IRAF is distributed by the National Optical Astronomy Observatories, which is operated by the Association of Universities for Research in Astronomy, Inc., under cooperative agreement with the National Science Foundation.

<sup>10</sup> Available at <http://obs.carnegiescience.edu/Code/python>.

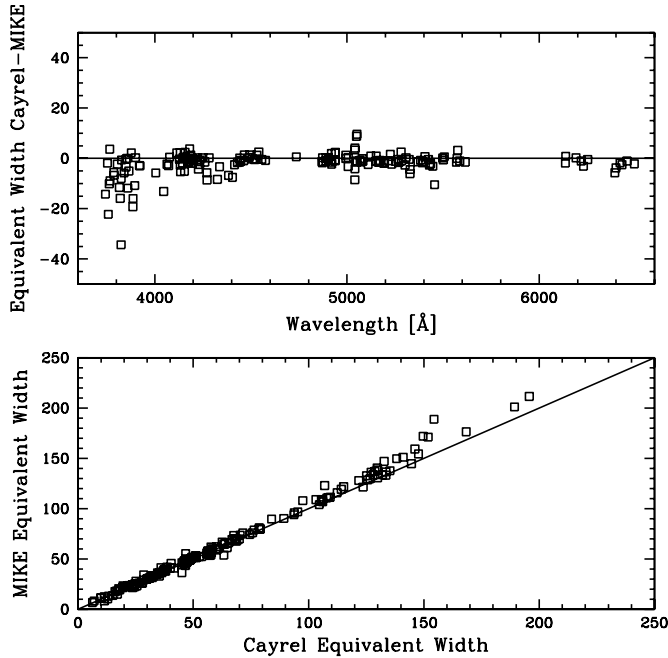


**Figure 2.** Comparison of the equivalent widths measured from the MIKE and Cayrel et al. (2004) spectra of BD -18 5550. In the upper panel, residuals of the equivalent widths (Cayrel–MIKE) are plotted against wavelength. In the bottom panel, the measured equivalent widths from Cayrel and MIKE are plotted against each other.

HRS spectra, the measured offset between the measurements shows no significant disagreement between the techniques.

### 3.3. Analysis Techniques

The large number of stars in the full  $\sim 500$  star CASH snapshot sample calls for automation of the analysis. Stellar parameters and elemental abundances from the snapshot HRS spectra were determined using our newly developed spectroscopic stellar parameter and abundance analysis pipeline, Cashcode. The pipeline is written around the existing platform of the local thermodynamic equilibrium (LTE) stellar line analysis and spectrum synthesis code MOOG (the latest version, 2010; Sneden 1973). The most recent version of MOOG accounts for

the fact that Rayleigh scattering becomes an important source of continuum opacity at short wavelengths, blueward of 4500 Å. This is important for our sample stars, as the effect is more pronounced in cool giants (Sobeck et al. 2011).

We compared the results of four representative stars, two from the pilot sample and two standard stars, using the newest version of MOOG and an older version that did not distinctly deal with Rayleigh scattering in the calculation of the continuum opacities. We find that the spectroscopic effective temperatures and microturbulences are lower; thus, the derived [Fe/H] abundances are lower by  $\sim 0.1$ – $0.2$  dex in the version that deals with Rayleigh scattering. Generally, the abundance ratios [X/Fe] remain within  $\sim 0.05$  dex. These abundances were determined using lines down to  $\sim 3750$  Å; however, for studies with a spectral range that encompasses shorter wavelengths, this effect may be larger. Table 3 shows the stellar parameter comparison and Table 4 shows the abundance ratio comparison.

## 4. STELLAR PARAMETERS

The first step in our abundance analysis is to determine the atmospheric parameters of each star. We accomplished this in two ways: with the Cashcode pipeline and the traditional, manual way.

In order to test the robustness of the snapshot abundances, one must answer two questions: first, for a given set of stellar parameters, with what precision can abundances be determined from snapshot spectra? Second, does the pipeline give reasonable stellar parameters (effective temperature, surface gravity, metallicity, and microturbulent velocity) for snapshot spectra? The first question has been partially answered by the HERES study, which finds that the uncertainties are  $\sim 0.25$  dex, but the systematic uncertainties associated with the stellar parameter and abundance determination methods and the inherent scatter of our snapshot data set must be explored. This is addressed in Section 6.6. The second question can be answered by testing the pipeline in detail and comparing the results from the literature with previously studied standard stars of comparable stellar parameters and metallicity; this is discussed in Section 6.7. Table 5 lists our adopted stellar parameters.

**Table 3**  
Stellar Parameter Comparison

Star	Scattering Treatment Included				No Scattering Treatment			
	$T_{\text{eff}}$ (K)	$\log g$	$\xi$ ( $\text{km s}^{-1}$ )	[Fe/H]	$T_{\text{eff}}$ (K)	$\log g$	$\xi$ ( $\text{km s}^{-1}$ )	[Fe/H]
HD 122563	4450	0.50	2.30	−2.96	4475	0.40	2.55	−2.85
CS 22891−200	4500	0.45	2.60	−3.93	4600	0.65	3.00	−3.72
HE 0015+0048	4600	0.90	1.85	−3.07	4675	1.05	2.15	−3.00
HE 0432−1000a	4525	0.50	2.00	−3.21	4600	0.65	2.60	−3.08

**Table 4**  
Abundance Comparison for Different Treatments of Scattering in MOOG

Element	CS 22891−200		HD 122653		HE 0015+0048		HE 0432−1000a	
	[X/Fe] <sub>scat</sub>	[X/Fe] <sub>non</sub>	[X/Fe] <sub>scat</sub>	[X/Fe] <sub>non</sub>	[X/Fe] <sub>scat</sub>	[X/Fe] <sub>non</sub>	[X/Fe] <sub>scat</sub>	[X/Fe] <sub>non</sub>
[Mg/Fe]	0.53	0.66	0.54	0.41	0.65	0.69	0.50	0.52
[Ca/Fe]	0.68	0.72	0.39	0.36	0.44	0.43	0.39	0.35
[Cr/Fe]	−0.43	−0.44	−0.18	−0.23	−0.17	−0.15	−0.15	−0.18
[Ni/Fe]	−0.08	−0.31	0.19	0.17	−0.02	0.05	0.01	0.16

**Table 5**  
Stellar Parameters

Star	MIKE				HRS			
	$T_{\text{eff}}$ (K)	$\log g$	$\xi$ ( $\text{km s}^{-1}$ )	[Fe/H]	$T_{\text{eff}}$ (K)	$\log g$	$\xi$ ( $\text{km s}^{-1}$ )	[Fe/H]
HE 0013–0257	4500	0.50	2.10	–3.82	4710	1.35	2.25	–3.40
HE 0013–0522	4900	1.70	1.80	–3.24	5120	2.30	2.00	–2.90
HE 0015 + 0048	4600	0.90	1.85	–3.07	4630	1.10	1.90	–3.00
HE 0302–3417a	4400	0.20	2.00	–3.70	...	...	...	...
HE 0324 + 0152a	4775	1.20	1.80	–3.32	4800	1.65	2.00	–3.05
HE 0420 + 0123a	4800	1.45	1.50	–3.03	4800	1.45	1.80	–3.00
HE 0432–1005a	4525	0.50	2.00	–3.21	4540	0.65	2.00	–3.10
HE 1116–0634	4400	0.10	2.40	–3.73	4650	1.00	3.80	–3.35 <sup>a</sup>
HE 1311–0131	4825	1.50	1.95	–3.15	4820	1.50	2.00	–2.85
HE 1317–0407	4525	0.30	2.15	–3.10	4600	0.25	3.20	–3.10 <sup>a</sup>
HE 2123–0329	4725	1.15	1.80	–3.22	4700	1.40	2.00	–3.05
HE 2138–0314	5015	1.90	1.75	–3.29	4940	2.30	2.00	–3.20
HE 2148–1105a	4400	0.20	2.65	–2.98	4450	0.20	3.20	–3.05 <sup>a</sup>
HE 2238–0131	4350	0.15	2.45	–3.00	4300	0.30	2.15	–3.05
HE 2253–0849	4425	0.20	2.65	–2.88	4420	0.15	2.30	–2.85
HE 2302–2154a	4675	0.90	2.00	–3.90	...	...	...	...
CS 22891–200	4500	0.45	2.60	–3.92	...	...	...	...
HD 122563	4450	0.50	2.30	–2.96	4400	0.30	2.25	–2.95
BD –18 5550	4600	0.80	1.70	–3.20	...	...	...	...
CD –38 245	4650	0.95	2.15	–4.00	...	...	...	...
CS 22873–166	4375	0.20	2.80	–3.14	...	...	...	...

**Note.** <sup>a</sup> Sky contamination in this spectrum.

#### 4.1. HRS Snapshot Data

The effective temperature of a star is spectroscopically determined by minimizing the trend of the relation between the abundance and excitation potential of the lines from which the abundance is derived. The microturbulent velocity is determined by doing the same for the abundance and reduced equivalent width. The surface gravity is determined from the balance of two ionization stages of the same element (e.g., Fe I and Fe II). The HRS snapshot spectra have few detectable Fe II lines; thus, we use Ti I and Ti II lines in addition to Fe I and Fe II lines in the pipeline to more robustly determine the stellar parameters, in particular the gravity, from these spectra, with Fe weighted twice compared to Ti. Often, only the ionization balance of Fe is considered. The metallicity used in the model atmosphere, in this case  $[M/H]$ , is an average of the abundances from individual lines of Fe I, Fe II, Ti I, and Ti II.

The pipeline works iteratively. The first process is to determine the stellar parameters from the equivalent width measurements of Ti I, Ti II, Fe I, and Fe II. An approximate initial guess to the effective temperature, surface gravity, metallicity, and microturbulent velocity is input as well as constraints on the parameters over which the code iterates. Generally, for the HRS snapshot data, we require that the trend between abundance and excitation potential is  $<|0.03|$  dex  $\text{eV}^{-1}$ , the reduced equivalent width and abundance trend is  $<|0.15|$  dex/ $\log(\text{m}\text{\AA})$ , the surface gravity criterion  $\Delta_{\text{ion}} < |0.10|$  dex, and the difference between the metallicity of the model atmosphere and the calculated metallicity is  $<|0.10|$  dex. As a result of the ionization balance constraints, the abundance difference between Ti I and Ti II is allowed to be no greater than 0.3 dex if the Fe I abundance equals the Fe II abundance or the abundance difference between Fe I and Fe II is allowed to be no greater than 0.2 dex if the Ti I abundance equals the Ti II abundance. This information is used to construct an initial Kurucz stellar atmosphere with

$\alpha$ -enhancement (Castelli & Kurucz 2004) to begin the stellar parameter determination, in which the pipeline iterates until the various constraints that determine each stellar parameter fall within the user-defined thresholds specified in the beginning.

We used the pipeline to derive abundances for each line from its equivalent width. We used synthetic spectra to determine abundances for particular lines (e.g., Ba II  $\lambda 4554$ ) for various reasons, including hyperfine structure and blending with other features. For these lines, we used an equivalent-width-derived abundance guess as an initial input for the spectral syntheses.

#### 4.2. High-resolution MIKE Spectra

The high-resolution MIKE data were analyzed manually. The large wavelength coverage allowed us to perform a more in-depth analysis with smaller uncertainties for a later comparison to the pipeline analysis of the corresponding snapshot spectra. Spectroscopic stellar parameters for all but two of the MIKE spectra were determined from equivalent width measurements of Fe I and Fe II lines. The resonance lines of Fe I were excluded in this analysis, as they often are near the flat portion of the curve of growth. In essence, all of the steps in the Cashcode pipeline were performed, but each step was executed manually. This allowed us to compare the pipeline results with those of a manual analysis to confirm that the pipeline reproduced the results derived from the high-resolution data.

It is also possible to determine effective temperatures photometrically, using calibrations between colors and temperature for given color and metallicity ranges. We have chosen to adopt spectroscopic temperatures for these stars, as well as for the entire CASH sample, in order to present a homogeneous set of atmospheric parameters and, therefore, the resulting chemical abundances. However, we determined photometric temperatures to check the accuracy and systematic uncertainties of our method. Accurate long baseline colors (i.e.,  $V - K$ ) for the entire  $\sim 500$  star sample do not exist; however, we used Two Micron

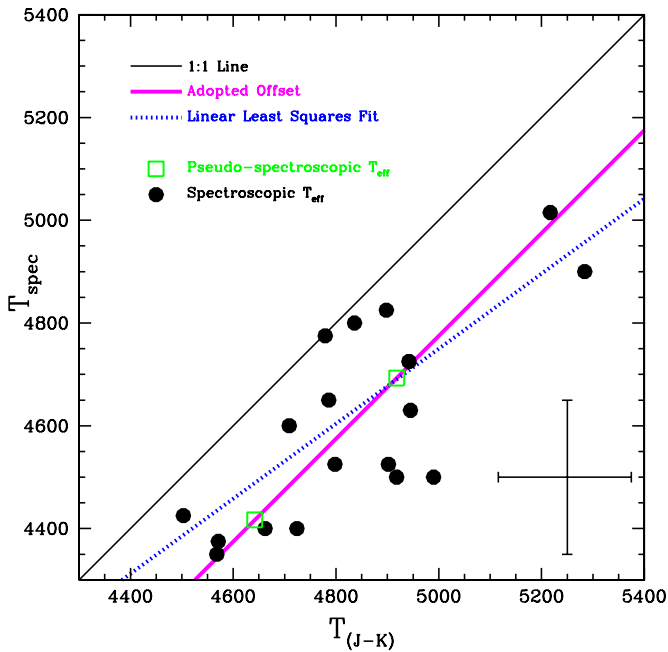


**Figure 3.** Comparison of the spectroscopic temperatures to those derived from  $(J-K)$  2MASS photometry using the Alonso et al. (1999) calibration. The thin black line is the 1:1 comparison, the dotted blue line is the linear least squares fit to the data, and the thick pink line shows the adopted offset applied to HE 1116–0634 and HE 2302–0317a, which are both represented by the green square points.

(A color version of this figure is available in the online journal.)

All Sky Survey (2MASS) photometry for the pilot sample and standard stars in order to determine photometric temperatures in order to compare them with the adopted spectroscopic temperatures.

We determined reddening corrections for our stars using the Schlegel et al. (1998) dust maps. We dereddened the  $J-K$  2MASS color and then, according to Equations (1a)–(1c) in Ramírez & Meléndez (2004), transformed  $J$  and  $K$  2MASS photometry into the Telescopio Carlos Sanchez system in order to use the Alonso et al. (1999) calibration to determine photometric temperatures. We determined the formal linear relation between the  $(J-K)$  photometric temperatures from the sample stars and the spectroscopic temperatures. Within the uncertainty of the fit, an offset exists between the spectroscopic and photometric temperatures. Thus, we adopted the mean difference between the spectroscopic and photometric temperatures to be  $T_{\text{spec}} = T_{(J-K)} - 225$  K. The uncertainties associated with the spectroscopic and photometric temperatures are 160 and 140 K, respectively. See the next subsection for further details. Figure 3 shows the spectroscopic temperature plotted against the  $(J-K)$  photometric temperature for the sample stars. Plotted are lines that show a 1:1 agreement, the adopted offset, and the least-squares fit.

Two stars in the sample, HE 1116–0634 and HE 2302–2154a, did not have convergent spectroscopic stellar parameter solutions irrespective of the analysis method. The Fe I and Fe II abundances were not in agreement (i.e., the surface gravity criterion was not met) when the temperature criterion was met. This is likely because these stars are near the edge of the stellar atmosphere grid in terms of metallicity, temperature, and gravity. For these stars, we adopted a “pseudo-spectroscopic” effective temperatures of 4400 and 4675 K for HE 1116–0634 and HE 2302–2154a, respectively. Those were obtained by applying

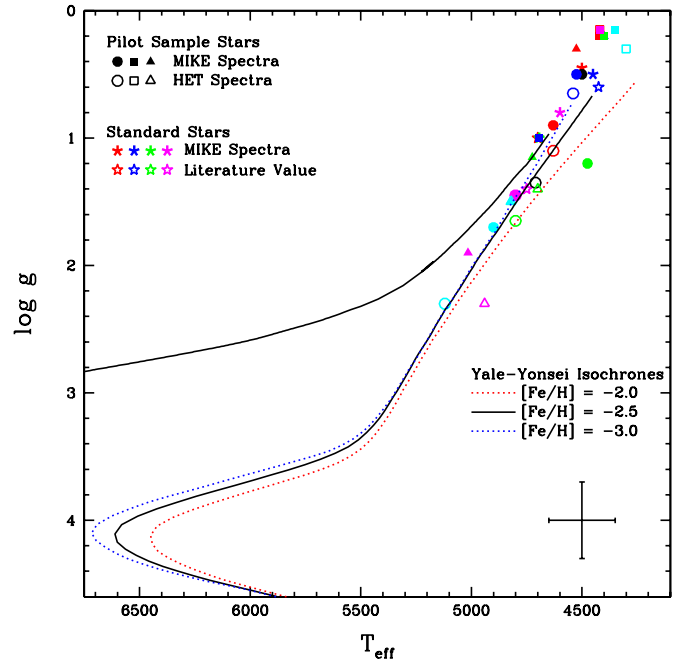


**Figure 4.** H-R diagram of the pilot sample and standard stars. For the pilot sample, open symbols represent the stellar parameters derived from the HRS spectra and the solid symbols represent stellar parameters derived from the MIKE spectra. For the standard stars, open stars represent stellar parameters derived from the MIKE spectra, and asterisks represent stellar parameters derived from the literature. Overplotted are the Yale-Yonsei isochrones (Green et al. 1984; Kim et al. 2002) for 12 Gyr, at  $[\text{Fe}/\text{H}] = -2.0$  (red line),  $-2.5$  (black line), and  $-3.0$  (blue line) as well as a horizontal-branch mass track from Cassisi et al. (2004).

(A color version of this figure is available in the online journal.)

the previously determined offset between the spectroscopic and photometric temperatures of 225 K to their photometric temperatures. The pseudo-spectroscopic temperatures were used to determine the remaining parameters, surface gravity, microturbulence, and metallicity spectroscopically, ignoring the nonzero slope of  $-0.065$  and  $-0.090$  dex  $\text{eV}^{-1}$  for HE 1116–0634 and HE 2302–2154a, respectively, of the excitation potential. Typically, this slope is  $<0.02$  dex  $\text{eV}^{-1}$ .

Figure 4 shows the derived effective temperatures and surface gravities for all stars in the sample plotted against 12 Gyr Yale-Yonsei isochrones (Green et al. 1984; Kim et al. 2002) for  $[\text{Fe}/\text{H}] = -2.0$ ,  $-2.5$ , and  $-3.0$ , as well as a Cassisi et al. (2004) horizontal-branch mass track. For the standard stars, we show the stellar parameters derived from the MIKE spectra, as well as literature values taken from Cayrel et al. (2004) for BD –18 5550, CD –38 245, and CS 22873–166, McWilliam et al. (1995) for CS 22891–200, and Fulbright (2000) for HD 122653. Due to the low-metallicity of CD –38 245, the corresponding MIKE spectrum shows very few absorption lines; thus, we included this star only in the calibration of the stellar parameter offset.

#### 4.3. Uncertainties

Each star has two or three measurements of temperature: spectroscopic temperatures derived from the MIKE and HRS spectra (when available) and a photometric temperature based on  $JHK$  2MASS colors using the Alonso et al. (1999) calibration.

We determined random uncertainties in the spectroscopic temperatures based upon the uncertainty in the slope determined by the Fe I line abundances. For a representative star, we

varied the temperature until the resultant Fe abundance was one standard deviation away from the original derived abundance. We found this value to be  $\sim 125$  K; we adopt this as our random uncertainty. We determined random uncertainties in the photometric temperatures based upon the uncertainties given for the 2MASS colors. We found this uncertainty to be  $\sim 140$  K.

We also compared the derived spectroscopic and photometric temperatures. Note that the offset between the two temperature scales is  $\sim 225$  K, where  $\Delta T_{\text{eff}} = T_{\text{eff}}^{\text{Phot}} - T_{\text{eff}}^{\text{Spec}}$ . Given this offset, we derive a systematic uncertainty for our spectroscopic temperatures of  $\sim 160$  K. This is of the same order as the random uncertainties.

We obtained the random uncertainty in the surface gravity by allowing the Fe I and Fe II values to vary until they no longer agree within the uncertainty of Fe I, which is  $\sim 0.25$  dex. Since all the pilot sample stars are on the giant branch, uncertainties in effective temperature at the  $\sim 150$  K level lead to changes in the surface gravities of  $\sim 0.5$  dex. We conservatively adopt this as our  $\sigma_{\log g}$  uncertainty.

We calculated the standard error of the mean Fe I abundance, obtained from individual Fe I line abundances and found it to be  $\sim 0.01$  dex. This is rather small, as the calculation does not take continuum placement uncertainties into account. With that in mind, we adopt the scatter of the individual Fe line abundances as a more conservative random [Fe/H] uncertainty, which is  $\sim 0.12$  dex, although it varies slightly by star.

In order to ascertain the uncertainty in the microturbulence, we determined the maximum change to the microturbulence values which would still yield the same [Fe/H] value within the uncertainties. This leads to  $\sigma_{\xi} \sim 0.3 \text{ km s}^{-1}$ .

## 5. ROBUSTNESS OF THE STELLAR PARAMETER AND ABUNDANCE PIPELINE

### 5.1. Stellar Parameters

One of the main purposes of this paper is to test the stellar parameter and abundance pipeline that will be used for the larger CASH sample. The first test is to compare the manually derived stellar parameter results with those determined with the Cashcode pipeline. This can be done in three ways: (1) comparing the stellar parameters and abundances of a manual analysis of a given spectrum with each Cashcode result; (2) comparing the results derived from snapshot spectra taken of standard stars with those of well determined literature values of the stellar parameters; and (3) comparing the stellar parameter results of a snapshot spectrum with those of a corresponding high-resolution spectrum.

We first tested the accuracy of the pipeline and the precision of our iteration criteria by comparing the results derived from a representative manual analysis of a high-resolution MIKE spectrum to those derived using the pipeline. We find  $\Delta T_{\text{eff}} = 10$  K,  $\Delta \log g = 0.0$ ,  $\Delta \xi = 0.05$ , and  $\Delta[\text{Fe}/\text{H}] = 0.02$  dex. We find that the [X/Fe] values (where X is a given element) agree to within  $\sim 0.05$  dex.

By comparing the Cashcode results of standard stars to the literature values, we can test how accurately the snapshot data are able to reproduce the results of independent studies derived from high-resolution, high-S/N data using traditional manual methods. We evaluated an absolute consistency between the Cashcode results and the literature. See Section 6.7 for details on the abundance differences. A caveat to this comparison is that standard stars are usually bright targets, such that their snapshot spectra have much higher S/N than the median

value for a snapshot spectrum. Generally, Cashcode produces abundance results with smaller uncertainties for higher-S/N, higher-resolution data because in these cases the line abundance scatter is decreased; therefore, the user-defined parameter fitting criteria can be tightened.

However, the purpose of this study is to test the pipeline for the median S/N snapshot star. Unfortunately, we did not observe a low-S/N snapshot spectrum of the standard stars, which precludes the best possible comparison. To resolve the issue, we instead turn to high-resolution data for testing the pipeline for a median S/N snapshot data. We compared the HRS pipeline-derived results to those of the manual, high-resolution analysis for all stars. We find agreement in the stellar parameters to be within  $\Delta T_{\text{eff}} \pm 55$  K,  $\Delta \log g \pm 0.3$  dex,  $\Delta[\text{Fe}/\text{H}] \pm 0.15$  dex, and  $\Delta \xi \pm 0.21$  dex.

### 5.2. Chemical Abundances

For each star with an HRS spectrum, we compared the derived abundances with the high-resolution MIKE spectrum. For the 12 stars in common, we found the offset between the two to have a standard error, or standard deviation of the mean, of 0.07 dex. The average  $\Delta[\text{X}/\text{Fe}]$  over all elements was 0.09 dex; thus, the abundances derived from the HRS data with Cashcode can reproduce a manual analysis to within  $1.5\sigma$ . Over all the elements, there is no statistically significant difference between the HRS/Cashcode and the MIKE/manual analysis. For individual elements, some discrepancies do exist. We found that the largest discrepancies between the HRS and MIKE spectra arose for those elements whose lines occurred in regions of low S/N (e.g., the  $\Delta[\text{X}/\text{Fe}]$  for Sr II is larger than that of Ba II, as the only Sr II line in the HRS occurs at 4215 Å, while there are Ba II lines at longer wavelengths).

For a given element, there is a discrepancy in the measured abundances derived from HRS and MIKE spectra. These range from 0.08 dex, in the case of Ti, which has nine lines across the HRS spectrum, to 0.36 dex, in the case of Sr, which has one feature at 4215 Å in the HRS spectrum. This value is dependent upon the location in wavelength and number of lines per element; bluer features from lower S/N spectral regions have larger discrepancies. Figure 5 illustrates the  $\Delta[\text{X}/\text{Fe}]$  for each element that was measured in both the HRS and MIKE spectrum of a particular star. We also compared the full set of [X/Fe] CASH- and MIKE-derived abundances to those of the Cayrel et al. (2004) study. Figure 6 shows the comparison between the three data sets. Manganese abundances are sometimes largely discrepant; however, this is likely because there are only four Mn lines available to detection in the HRS spectra and often only one of these lines was detected. It has been previously noted (Cayrel et al. 2004; Roederer et al. 2010) that the line selection for Mn is critical in understanding the derived abundances and the Cayrel et al. (2004) study included additional lines not available in the HRS spectra.

## 6. ABUNDANCE ANALYSIS

We present chemical abundances and upper limits for 13 elements derived from the HRS spectra and 18 elements from the MIKE spectra in Table 6. We now describe the details of our abundance analysis. For each element, we discuss the method of abundance determination, the relevant spectral features, the number of stars in which this element was measured, and any differences in the analysis between the high-resolution and snapshot spectra.



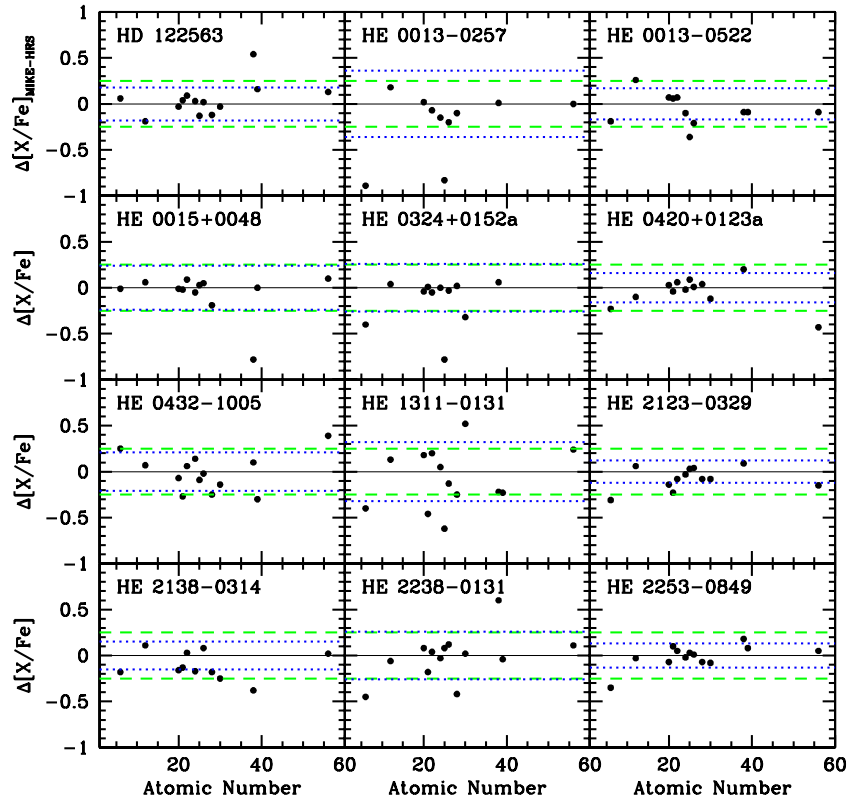


**Figure 5.** Abundance differences,  $\Delta[X/Fe]$ , defined as  $[X/Fe]_{\text{MIKE}} - [X/Fe]_{\text{HRS}}$ , shown as a function of atomic number for each star that was observed with both HRS and MIKE. The black solid line represents zero offset, the green dashed line represents the 0.25 dex random spread derived in the HERES study, and for comparison, the blue dotted line represents the calculated spread for each star.

(A color version of this figure is available in the online journal.)

**Table 6**  
Abundances

Element	$\log\epsilon(X)$ (dex)	[X/Fe]	$\sigma$	$n$	[X/Fe]
		MIKE	(dex)		HRS
		HE 0015-0048			
Mg I	5.18	0.66	0.18	6	0.62
Ca I	3.71	0.45	0.14	15	0.44
Sc II	0.14	0.07	0.14	8	0.06
Ti I	1.98	0.11	0.18	18	0.11
Ti II	2.14	0.27	0.15	39	0.06
Cr I	2.40	-0.16	0.20	14	-0.14
Mn I	2.06	-0.29	0.14	4	-0.28
Co I	1.97	0.06	0.14	6	...
Ni I	3.13	-0.01	0.16	8	...
Zn I	1.58	0.10	0.14	1	0.68
Sr II	-1.06	-0.87	0.14	2	-0.39
Ba II	-2.07	-1.17	0.14	3	-1.30

(This table is available in its entirety in a machine-readable form in the online journal. A portion is shown here for guidance regarding its form and content.)

### 6.1. Light Elements: Li, C, Al, Si

Lithium abundances were determined from both the HRS and MIKE spectra through synthesis of the Li I doublet at 6707 Å. Both spectra cover this feature. Lithium is most easily detected in main-sequence stars, but as a star ascends the red giant branch (RGB), its Li abundance becomes depleted. Thus, we only expect to detect the Li feature in our warmest giants. We detected the doublet in 5 of 12 stars with HRS spectra and 7 of 20 stars with MIKE spectra.

Carbon abundances were determined from the CH *G*-band feature at 4313 Å. The S/N near the *G*-band head region in the HRS snapshot spectra is low, such that we have to perform a manual synthesis of the *G*-band head in order to determine the C abundances. At low S/N, Cashcode does not yield reliable results mostly due to uncertainties in continuum placement. For synthesis we assumed an [O/Fe] abundance ratio of 0.0. When the [O/Fe] ratio reaches  $\sim 1$ , the C abundances determined from molecular features are affected, though none of our stars indicate such a high O abundance. We detected this feature in all stars in both sets of spectra. The two available O indicators in our spectra are the forbidden line at 6300 Å and the O triplet. At the metallicity of our sample, we are unable to detect the forbidden line except for cases of extreme O enhancement. The triplet lines are known to have non-LTE (NLTE) effects and thus we did not measure an O abundance.

Sodium abundances were not included in this analysis as we have not implemented a routine in the pipeline to discern the stellar absorption lines from the interstellar emission.

Aluminum abundances were determined using equivalent width measurements of the  $\lambda 3961$  line of the Al I resonance doublet. We opted to use only the  $\lambda 3961$  line for our abundance analysis because the other line,  $\lambda 3944$ , is blended with CH. Neither feature falls within the HRS snapshot wavelength regime. We measured this line in 19 of the MIKE spectra. We did not measure the Al abundance in HD 122563 due to the low S/N of that spectrum.

Two Si lines are detectable in metal-poor stars:  $\lambda 3906$  and  $\lambda 4103$ . The  $\lambda 3906$  line is heavily blended with CH in a low-

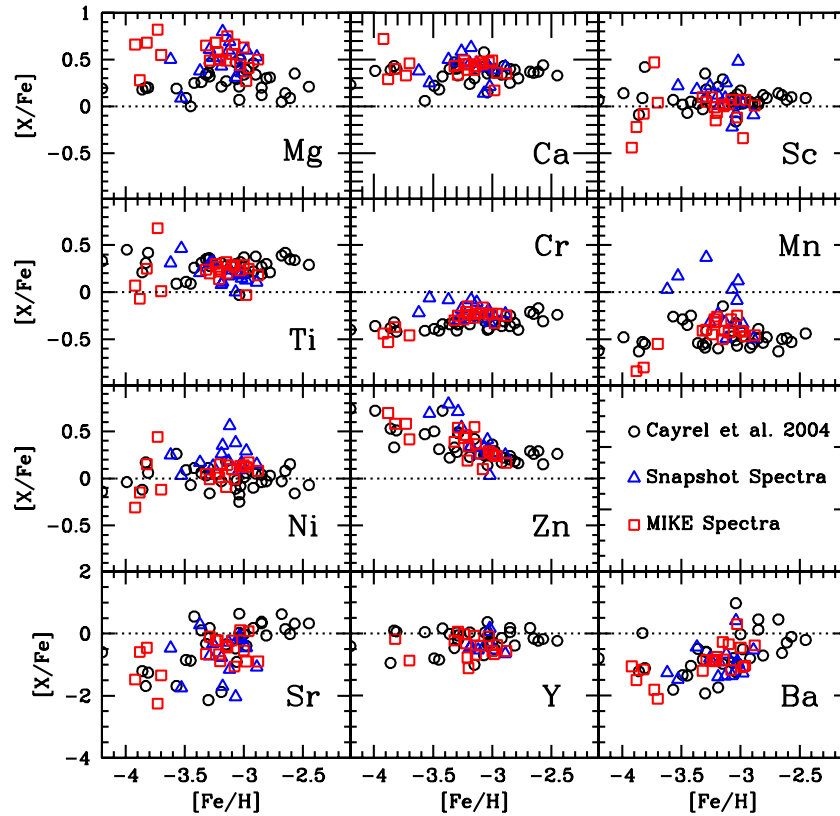


**Figure 6.**  $[X/Fe]$  abundance ratios vs.  $[Fe/H]$  for each of the elements measured using Cashcode in the HRS snapshot spectra (blue triangles) compared with the MIKE abundances (red squares) and the Cayrel et al. (2004) abundances (black circles). The black dotted line represents the solar abundance ratio. The HRS Ni abundances shown are preliminary.

(A color version of this figure is available in the online journal.)

S/N region of the spectrum; however, we prefer to use only unblended lines for our analysis. The  $\lambda 4103$  line falls within the wing of the  $H\delta$  line; thus, we adopt a local continuum in the wing of the  $H\delta$  line. We present spectral synthesis derived abundances from the MIKE spectra using the  $\lambda 4103$  line. Neither feature is available in the snapshot spectra due to limited wavelength coverage. We measured this line in 19 stars with MIKE spectra.

### 6.2. $\alpha$ -Elements: Mg, Ca, Ti

Abundances for Mg, Ca, and Ti were determined for all stars in the sample from both the HRS and MIKE spectra from equivalent width analysis. Only four unblended Mg I lines are available in the HRS snapshot spectra:  $\lambda 4703$ ,  $\lambda 5173$ ,  $\lambda 5184$ , and  $\lambda 5528$ . The Mg b lines are often near the flat part of the curve of growth, but their abundances generally agree with those of the abundances of the other two lines. Thus, they were included in the abundance determination. There are  $\sim 12$  detectable lines in the MIKE spectra, although in these spectra we exclude lines on the flat part of the curve of growth. This is determined on a line-by-line basis for each star.

There are four Ca I lines available in the snapshot spectra:  $\lambda 5589$ ,  $\lambda 6103$ ,  $\lambda 6122$ ,  $\lambda 6162$ . Of the four lines, the last three lines are sometimes blended with telluric features. This was assessed on a line-by-line basis in each star. There are  $\sim 30$  Ca I lines in the MIKE spectra. Although the Ca I  $\lambda 4226$  line is available in the HRS spectra, we did not include it in our analysis because of the low S/N of the feature. Additionally, this line is often excluded from the MIKE analysis because it is in the flat part of the curve of growth.

Titanium abundances were determined from six Ti I and nine Ti II lines in the snapshot spectra and  $\sim 30$  Ti I lines and  $\sim 60$  Ti II in the high-resolution spectra.

### 6.3. Fe-Peak Elements: Sc, Cr, Mn, Co, Ni, Zn

All abundances were determined from equivalent width measurements except for Zn because it has only two weak lines. There are four detectable Sc II lines in the snapshot data:  $\lambda 5031$ ,  $\lambda 5239$ ,  $\lambda 5526$ , and  $\lambda 5657$ . There are  $\sim 15$  Sc II lines detectable in the MIKE spectra. We detected Sc lines in 20 MIKE spectra and 11 HRS spectra.

We measured five Cr I lines in the snapshot spectra:  $\lambda 4616$ ,  $\lambda 4646$ ,  $\lambda 5206$ ,  $\lambda 5346$ , and  $\lambda 5410$ . We measured  $\sim 20$  Cr I lines and four Cr II lines in the MIKE spectra:  $\lambda 3409$ ,  $\lambda 4559$ ,  $\lambda 4588$ , and  $\lambda 4592$ . There is a difference between the abundances derived between Cr I and Cr II, with Cr II abundances typically  $\sim +0.35$  dex larger than Cr I. We detected the Cr I lines in 19 MIKE spectra and 12 HRS spectra. In all plots, we adopt the  $[Cr I/Fe]$  values as  $[Cr/Fe]$ .

We measured four Mn I lines in the HRS spectra— $\lambda 4754$ ,  $\lambda 4762$ ,  $\lambda 4783$ , and  $\lambda 4823$ —and eight Mn I lines in the MIKE spectra. We detected Mn I lines in 19 MIKE spectra and 11 HRS spectra.

In the MIKE data we measured  $\sim 30$  Ni I lines, but only the  $\lambda 5477$  and  $\lambda 6177$  Ni I lines are available in the HRS spectra. Abundances derived from the  $\lambda 5477$  line sometimes are erroneously large by  $\sim 0.2$  dex. We will develop a calibration for the large CASH sample, but here we only report Ni abundances derived from the MIKE spectra for all 20 stars.

We measured 11 Co I lines in the MIKE spectra that fall between 3502 Å and 4122 Å. These lines are not covered by the snapshot spectra. We detected Co I lines in all 20 MIKE spectra.

Zinc abundances were determined via spectral synthesis of the  $\lambda 4722$  and  $\lambda 4810$  Zn I lines in both the HRS and MIKE spectra. We detected Zn I lines in 19 MIKE spectra and 9 HRS spectra.

#### 6.4. Neutron-capture Elements

We measured abundances for six neutron-capture elements via spectral synthesis. The Sr II  $\lambda 4215$  and  $\lambda 4077$  lines are covered by the MIKE spectra, while only the  $\lambda 4215$  line is available in the HRS spectra. We detected Sr II lines in all stars in both the HRS and MIKE spectra.

We synthesized the  $\lambda 4883$  and  $\lambda 5087$  Y II lines in the HRS snapshot spectra and the  $\lambda 3949$  and  $\lambda 4883$  lines in the MIKE spectra. The  $\lambda 3949$  line was chosen because it is a prominent line and can still be detected when a giant star has sub-solar neutron-capture abundances. We excluded the  $\lambda 5087$  line because it falls in a region in the MIKE spectra with low S/N, as it is at the edge of both the blue and red edges of the CCD. We detected Y II lines in 16 MIKE spectra and 6 HRS spectra. We report upper limits from the MIKE spectra for five stars.

We synthesized the Zr II  $\lambda 4209$  line to determine the abundance for the MIKE spectra. Even though this line is available in the HRS snapshot spectra, the S/N in the blue region of all spectra is too low for such a weak feature. We detected the line in 12 MIKE spectra. We report upper limits from the MIKE spectra for nine stars.

For the HRS spectra, we used three Ba II lines:  $\lambda 4554$ ,  $\lambda 5854$ , and  $\lambda 6142$ ; however, often only the  $\lambda 4554$  line can be measured given the low S/N of the HRS data as well as the low metallicity of the sample. The same lines were measured in the MIKE spectra, with the addition of the  $\lambda 6496$  line. Generally, these weaker lines are preferable because the  $\lambda 4554$  line is usually on the damping part of the curve of growth, especially in neutron-capture-enhanced stars. We measured Ba in 20 MIKE spectra and 11 HRS spectra.

We synthesized two La II lines at 4086 and 4123 Å in the MIKE spectra. The HRS spectra do not cover these wavelengths.

We synthesized two Eu II lines at 4129 and 4205 Å in the MIKE spectra. The HRS spectra do not cover these wavelengths. We detected La II and Eu II features in the five same stars in the MIKE spectra. We report upper limits from the MIKE spectra for 15 stars for both Eu and La.

#### 6.5. Non-LTE Effects

Chemical abundances are generally derived under the assumption of 1D model atmospheres in LTE, but non-LTE effects may alter our derived values. The non-LTE effects in the elements Mg, Sr, and Ba have been studied in the stars of the Cayrel et al. (2004) sample by Andrievsky et al. (2010), Andrievsky et al. (2011), and Andrievsky et al. (2009), respectively. Based on their reanalysis of the Cayrel et al. (2004) sample, the non-LTE corrections would be  $\sim 0.15$  for Mg and Ba in our sample. In the case of Sr, the non-LTE abundances vary, and can be larger and smaller than the LTE abundances even for stars of similar temperature and gravity, so it is difficult to say what this effect would be in our stars. See also Asplund (2005) for a comprehensive review of non-LTE effects on stellar abundances for a range of elements. Such effects are very sensitive to stellar parameters and individual lines from which the abundances are derived. In the absence of “full grid” non-LTE correction calculations, we

are not able to apply such corrections to our sample; however, note that these corrections have implications for interpretations of Galactic chemical evolution models and should be taken into account for such investigations. To illustrate the magnitude of non-LTE effects, we discuss Al and Mn here, as both have some of the most severe non-LTE corrections.

Baumüller & Gehren (1997) present a non-LTE-corrected [Al/H] abundance analysis for four sets of stars for the  $\lambda 3961$ ,  $\lambda 6696$ ,  $\lambda 6698$ ,  $\lambda 8772$ , and  $\lambda 8773$  lines. Only the first line is detected in stars with  $[\text{Fe}/\text{H}] < -2.0$ , and thus applicable to this study. The  $\lambda 3944$  line is also detectable in metal-poor stars, but it is blended with CH features. They calculated non-LTE abundances for 6500 K and 5200 K main-sequence stars, a 5780 K solar analog, and a 5500 K turn-off star, with  $[\text{Fe}/\text{H}]$  varying from  $-3.00$  to  $0.00$  dex. For a given set of atmospheric parameters, the  $[\text{Al}/\text{H}]_{\text{NLTE}}$  correction increases with decreasing  $[\text{Fe}/\text{H}]$ . The most evolved star ( $T_{\text{eff}} = 5500$  K,  $\log g = 3.5$ ) in their analysis has a non-LTE correction of 0.65 dex. All the stars of the pilot sample are on the giant branch and generally are more metal-poor than the Baumüller & Gehren (1997) models, which indicates that our stars would have a larger non-LTE correction for the  $\lambda 3961$  line, though they would likely all have a similarly large correction.

Bergemann & Gehren (2008) note that Mn has strong non-LTE effects, which increase with decreasing metallicity. These effects have been shown to be stronger in the  $\lambda 4030$  resonance triplet, which we do not include in our analysis. The most evolved, metal-poor model analyzed in Bergemann & Gehren (2008) ( $T_{\text{eff}} = 5000$  K,  $\log g = 4$ ,  $[\text{Fe}/\text{H}] = -3$ ) has an average  $[\text{Mn}/\text{Fe}]$  non-LTE correction of 0.42 dex for the lines that we include in our Mn line list ( $\lambda 4030$ ,  $\lambda 4033$ ,  $\lambda 4034$ ,  $\lambda 4041$ ,  $\lambda 4754$ ,  $\lambda 4783$ , and  $\lambda 4823$ ). They also included HD 122563 in their sample of stars and calculated a non-LTE correction of +0.44 dex to the  $[\text{Mn}/\text{Fe}]$  ratio. Again, we do not adopt a non-LTE correction for any of our sample, though corrections of this magnitude would indicate that our average  $[\text{Mn}/\text{Fe}]$  trend is elevated to a slightly sub-solar level. The aforementioned elements have large non-LTE corrections, though other elements do not have corrections of this magnitude; thus, their abundances can be used for interpretation in a straightforward manner.

#### 6.6. Uncertainties

To determine the random uncertainty of our abundances, we calculated the scatter of the individual line abundances for each ionization state of each element measured. For any abundance determined from equivalent width measurements of less than 10 lines, we determined an appropriate small sample adjustment for  $\sigma$  (Keeping 1962). In the case of any abundance uncertainty that was calculated to be less than the uncertainty in the Fe I lines, we conservatively adopted the value from Fe I for that particular star. Typically, the Fe I uncertainty is  $\sim 0.12$  dex.

For those lines with abundances determined via spectral synthesis, we determined abundance uncertainties based on the uncertainties associated with equivalent width measurements. Continuum placement is the greatest source of uncertainty, along with the S/N of the region containing the particular line. Most of these abundances were determined from only two lines; thus, we calculated the uncertainties for small samples. For those elements with only one line, we adopt the uncertainties determined for the Fe I abundance.

To obtain the systematic uncertainties in the abundances, we redetermined abundances by individually varying the stellar parameters by their adopted uncertainties. We chose a nominal

**Table 7**  
Example Systematic Abundance Uncertainties for HE 0015+0048

Element	$\Delta T_{\text{eff}}$ (+150 K)	$\Delta \log g$ (+0.5 dex)	$\Delta \xi$ (+0.3 km s <sup>-1</sup> )
CH	0.35	-0.20	0.00
Mg I	0.11	0.06	-0.04
Al I	0.17	0.18	0.11
Si I	0.15	-0.05	-0.05
Ca I	0.13	0.06	0.04
Sc II	0.07	-0.15	-0.05
Ti I	0.23	0.06	-0.02
Ti II	0.05	-0.14	-0.08
Fe I	0.18	-0.05	-0.05
Fe II	-0.01	0.15	-0.06
Cr I	0.21	0.08	-0.10
Mn I	0.21	0.08	-0.14
Co I	0.24	0.06	-0.11
Ni I	0.21	0.09	-0.17
Zn I	0.00	0.00	-0.05
Sr II	0.10	0.10	-0.20
Ba II	0.10	0.10	-0.07

value of 150 K for the effective temperature uncertainty, as this value is similar to the random and systematic uncertainties. Table 7 shows these results. We find that the effective temperature contributes most to the abundance uncertainty. The uncertainty in the surface gravity is somewhat less significant for most species. For elements with particularly strong lines, especially those whose abundances are determined with spectral synthesis, the microturbulence can be an important source of error.

### 6.7. Standard Stars

We compared our stellar parameters and [X/Fe] abundances for our four standard stars (HD 122563, BD -18 5550, CS 22873-166, and CS 22891-200) against three studies: McWilliam et al. (1995), Fulbright (2000), and Cayrel et al. (2004). We also compared our derived stellar parameters for CD -38 245 with those of McWilliam et al. (1995). The McWilliam et al. (1995) study differs from the other two and this study as those spectra had comparatively low S/N (~35). These stars were chosen from the literature because they have [Fe/H] ~ -3 or below and are in similar evolutionary stages. Table 8 lists the stellar parameters derived in all three studies, as well as ours, for the five stars, and Table 6 includes the derived abundances.

The McWilliam et al. (1995) study contains four stars (including CD -38 245) which overlap with our study. That work utilized model atmospheres from Kurucz (1993) with MOOG. We use an updated version of this code, which explicitly deals with Rayleigh scattering as a continuum opacity source; see paragraph 1 in Section 3.3. The effective temperatures for this study were derived from photometry, with the microturbulence determined from Fe I lines and the surface gravity determined from the ionization balance of Fe I and Fe II lines. We find that our temperatures are lower by ~170 K. Our derived surface gravities are also lower, as a result of the lower temperatures. We also find a ~ -0.3 dex offset in the [Fe/H] values. The cause of these discrepancies is likely twofold: the different temperature scales and how the most recent version of MOOG explicitly deals with the Rayleigh scattering opacity (see Table 3). Both lead to lower temperatures, surface gravities, and abundances.

Despite these absolute offsets, the derived abundance ratios have only small offsets, with the average offset between the two studies in  $\langle \Delta[X/\text{Fe}] \rangle$  for all three stars being  $0.04 \pm$

**Table 8**  
Literature Values for Stellar Parameters

Study	$T_{\text{eff}}$ (K)	$\log g$	[Fe/H]	$\xi$ (km s <sup>-1</sup> )
HD 122563				
This study	4450	0.50	-2.96	2.30
Fulbright	4425	0.60	-2.79	2.05
McWilliam	...	...	...	...
Cayrel	4600	1.10	-2.82	2.00
BD -18 5550				
This study	4600	0.80	-3.20	1.70
Fulbright	...	...	...	...
McWilliam	4790	1.15	-2.91	2.14
Cayrel	4750	1.40	-3.06	1.80
CD -38 245				
This study	4560	0.95	-4.35	2.15
Fulbright	...	...	...	...
McWilliam	4730	1.80	-4.01	1.97
Cayrel	4800	1.50	-4.19	2.20
CS 22873-166				
This study	4375	0.20	-3.14	2.60
Fulbright	...	...	...	...
McWilliam	4480	0.80	-2.90	3.01
Cayrel	4550	0.90	-2.97	2.10
CS 22891-200				
This study	4500	0.45	-3.92	2.60
Fulbright	...	...	...	...
McWilliam	4700	1.00	-3.49	2.51
Cayrel	...	...	...	...

**References.** Fulbright (2000), McWilliam et al. (1995), Cayrel et al. (2004).

0.24 dex, where  $\Delta[X/\text{Fe}]$  is  $[X/\text{Fe}]_{\text{Standard}} - [X/\text{Fe}]_{\text{MIKE}}$ . For all three stars, Al and Si had the largest offsets, where McWilliam et al. (1995) derive systematically higher abundances. The Al abundances for McWilliam et al. (1995) may generally be high, as they were found to be higher ( $\Delta[\text{Al}/\text{Fe}] \sim 0.5$  dex) than Gratton & Sneden (1988), with no conclusion for the cause of the offset being reached. The Al and Si lines are located in low-S/N regions in both studies; however, the measurement of the Al lines is difficult due to the suppression of the continuum from Ca H and K lines. As stated in Baumüller & Gehren (1997), even under the assumption of LTE, small changes in the effective temperature and surface gravity greatly change the line profiles. In addition, the proximity of the H $\delta$  line produces larger uncertainties in our Si measurement, even when the feature is taken into account in the synthetic spectra. These reasons would produce a larger scatter in the measurements of Al and Si lines, compared to the other elements, and may explain the derived abundance discrepancy. When these two elements are removed from consideration,  $\langle \Delta[X/\text{Fe}] \rangle$  becomes  $-0.02 \pm 0.13$  dex.

The only star that overlaps with the Fulbright (2000) study is HD 122563, though this particular study was chosen because the stellar parameters were determined spectroscopically, in the same manner as the stellar parameters determined from the MIKE spectra. Fulbright (2000) used Kurucz (1993) model atmospheres with MOOG as well. We found that the effective temperatures, surface gravities, and microturbulence values agree within the uncertainties associated with both studies, while  $\Delta[\text{Fe}/\text{H}]$  is  $-0.17$  dex. Similar to the effects seen in comparison with the McWilliam et al. (1995) study, this is due to the fact that the version of MOOG used in the Fulbright (2000) study did not explicitly handle the calculation

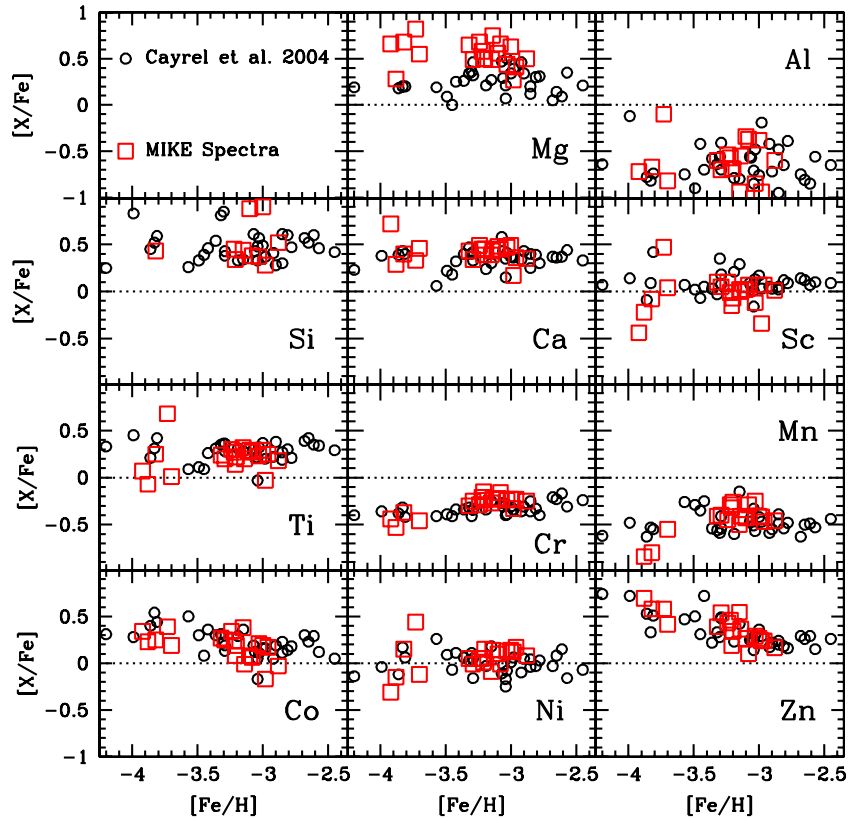


**Figure 7.**  $[X/Fe]$  abundance ratios vs.  $[Fe/H]$  for each of the elements up to Zn manually measured in the MIKE spectra (red squares) compared with the Cayrel et al. (2004) abundances (black squares). The black dotted line represents the solar abundance ratio.

(A color version of this figure is available in the online journal.)

of scattering from pure absorption in terms of the continuum opacity.

The derived abundance ratios are in good agreement, with  $\langle \Delta[X/Fe] \rangle = 0.02 \pm 0.09$  dex. The largest discrepancy lies with the  $[Mg/Fe]$  ratio, with  $\Delta[Mg/Fe] = 0.20$  dex, which was derived with a different set of lines and different oscillator strengths between this study and the Fulbright (2000) study.

The Cayrel et al. (2004) study has four stars in common with ours (including CD -38 245). This study uses OSMARCS atmospheric models with the LTE synthetic spectrum code “turbospectrum,” which explicitly handles the calculation of the scattering contribution with regard to the continuum opacity. The effective temperatures were determined via  $(V-K)$  colors, which leads to higher temperatures ( $\sim 200$  K) and surface gravities ( $\sim 0.6$  dex) compared to our spectroscopically derived stellar parameters. We ran the measured equivalent widths of Cayrel et al. (2004) for BD -18 5550 through Cashcode and found that our derived stellar parameters (4560 K, 0.6 dex,  $-3.22$ , and  $1.7 \text{ km s}^{-1}$  in effective temperature, surface gravity,  $[Fe/H]$ , and microturbulence, respectively) were in agreement ( $\Delta[Fe/H] = 0.02$  dex).

In comparing the  $[X/Fe]$  values between our analysis of the Cayrel et al. (2004) equivalent widths and theirs, we find that our spectroscopically derived stellar parameters also lead to higher  $[Mg/Fe]$  values by  $\sim 0.25$  dex due to the gravity-sensitive nature of the Mg lines.

The derived abundance ratios also agree well, with  $\langle \Delta[X/Fe] \rangle = -0.03 \pm 0.14$  dex. The largest sources of discrepancy for all stars are Al and Si, in addition to Mg. In CS 22873-166, there is a 0.45 discrepancy between the  $[Sr/Fe]$  values. The S/N near both lines in the MIKE spectrum is  $\sim 20$ .

Additionally, the lines are very strong, making continuum placement a large source of uncertainty, as minor adjustments to the continuum level result in large changes in the abundance.

## 7. ABUNDANCE RESULTS AND DISCUSSION

Table 6 lists abundance results derived from the MIKE spectra. Figure 6 shows the  $[X/Fe]$  abundance ratios of all elements derived from the HRS spectra, plotted with the Cayrel et al. 2004 and MIKE abundance ratios for comparison. Figures 7 and 8 include the  $[X/Fe]$  abundance ratios derived from the MIKE spectra, plotted against  $[Fe/H]$  for all stars in the sample. These abundance ratios are overplotted against the Cayrel et al. (2004) abundances as a point of comparison. The table also includes the abundances derived from the HRS spectra, though we do not discuss these further. These abundances will later be included in the full  $\sim 500$  star CASH sample. For each element, Table 9 lists the parameters of a least-squares linear trend versus metallicity, the abundance scatter, and the average  $[X/Fe]$  value, if applicable.

### 7.1. Light Elements

We detected Li in six of our stars: HE 0324+0152a, HE 0420+0123a, HE 1311-0131, HE 2123-0329, HE 2138-0314, HE 2302-0849a, and in one standard star, BD -18 5550. These detections were seen in both the snapshot and high-resolution spectra for HE 0420+0123a, HE 1311-0131, HE 2123-0329, and HE 2138-0314. BD -18 5550 and HE 2302-0849 do not have a corresponding snapshot spectrum. In Figure 9, we show the Li line in the HRS and MIKE data for all these stars. Otherwise, we determined upper limits. In each

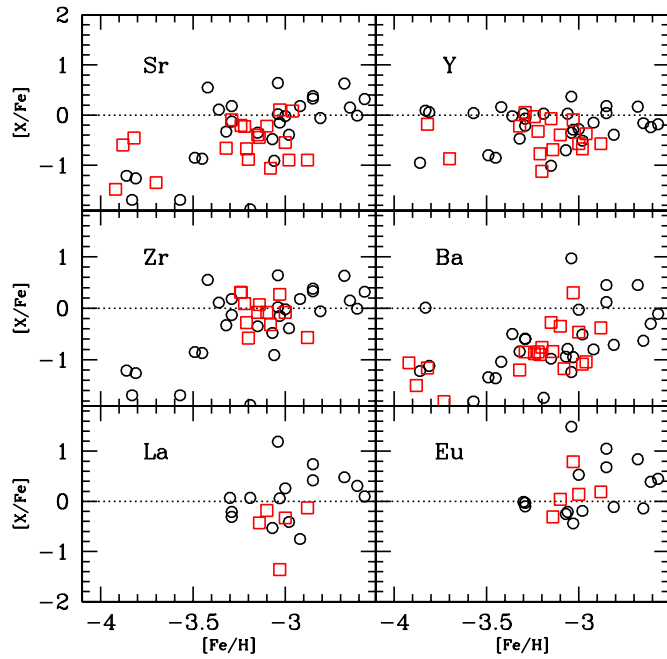


**Figure 8.**  $[X/Fe]$  abundance ratios vs.  $[Fe/H]$  for six neutron-capture elements measured in the MIKE spectra (red squares) compared with the Cayrel et al. (2004) abundances (black circles). The black dotted line represents the solar abundance ratio.

(A color version of this figure is available in the online journal.)

**Table 9**  
Summary of Abundance Trends

Element	$\langle [X/Fe] \rangle$	Slope vs. $[Fe/H]$	$\sigma$	$n_{\text{stars}}$
CH	0.02 <sup>a</sup>	-0.52 <sup>b</sup>	0.41	20
Mg I	0.56	...	0.14	20
Al I	...	0.11	0.22	19
Si I	...	-0.20	0.16	19
Ca I	0.42	...	0.11	20
Ti II	0.22	...	0.16	20
Sc II	...	...	0.19	20
Cr I	...	0.26	0.02	19
Mn I	-0.49	0.24	0.09	19
Co I	0.42	...	0.11	20
Ni I	0.05	...	0.15	20
Zn I	...	-0.42	0.04	19
Sr II	-0.66	...	0.57	20
Y II	-0.46	...	0.32	15
Zr II	-0.08	...	0.26	11
Ba II	-0.95	...	0.25	20

**Notes.**

<sup>a</sup> Average  $[C/Fe]$  value calculated for non-CEMP stars.

<sup>b</sup> Slope calculated for  $\log(L/L_{\odot})$  vs.  $[C/Fe]$ . See Figure 11.

case, the S/N of the region was measured and the corresponding  $3\sigma$  upper limit on the equivalent width was calculated following Bohlin et al. (1983) and Frebel et al. (2007b). Figure 10 shows the Li abundance as a function of metallicity and effective temperature, along with the Hertzsprung–Russell (H-R) diagram of the stars with detected Li.

The Spite plateau (Spite & Spite 1982) is an observational discovery that describes a constant Li abundance in low-metallicity stars near the main-sequence turn-off. Metal-poor stars near or on the main sequence have not yet burned their surface Li; it is therefore thought that the stars that populate the Spite plateau can be used to infer details about the primordial

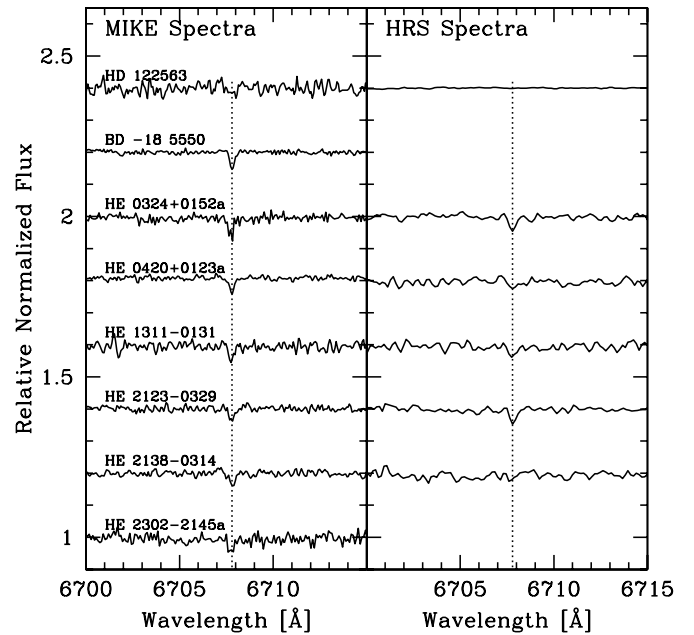


**Figure 9.** Li  $\lambda 6707$  line detections in MIKE (left panel) and CASH (right panel). Plotted (dashed line) is the location of the feature. Also included for comparison is HD 122563, a star for which no Li was detected.

Li abundance. As stars evolve off the main sequence and up the RGB, their convection zone deepens and the atmospheric Li abundance is depleted through burning and convective dredge up. Any enhancement in the Li abundance (e.g., Roederer et al. 2008) is likely from some form of Li synthesis that occurs during the course of stellar evolution, perhaps due to the Cameron–Fowler mechanism (Cameron & Fowler 1971). All of the stars in the pilot sample are on the giant branch and, thus, are expected to have depleted Li abundances. Due to the evolutionary status of the pilot sample, we cannot comment on the nature of the Spite plateau. Accurate Li abundances require great care in the effective temperature determination, as the Li abundance is extremely temperature sensitive. Most Li abundance studies (e.g., Ryan et al. 1996; Asplund et al. 2006; García Pérez & Primas 2006; Bonifacio et al. 2007; Meléndez et al. 2010) employ long baseline (e.g.,  $V-K$ ) photometric effective temperatures. Keeping the different temperature scales in mind, we find that our abundances qualitatively fall along an extrapolation of the Ryan & Deliyannis (1998) Li dilution curve.

Figure 11 shows a plot of our derived  $[C/Fe]$  abundances against  $[Fe/H]$  and luminosity. The Cayrel et al. (2004) abundances are also shown for reference. The abundance offset as a function of luminosity between the two samples is due to the different temperature scales used, as also quantified in Table 7. Generally, we find a large spread in the  $[C/Fe]$  abundance ratios, from  $\sim -0.80$  to  $\sim 0.8$  dex, with  $\sigma = 0.41$  dex. In Figure 12, we show spectra for two stars of similar temperature ( $\sim 4550$  K) that differ in  $[C/Fe]$  by  $\sim 1.0$  dex.

However, the interpretation of the observed  $[C/Fe]$  ratio must be carefully evaluated. As stars evolve up the RGB, the C abundance drops due to CN cycling and convective dredge up. Thus, we expect that the observed C abundances derived for our stars should be lower than their initial abundances. Gratton et al. (2000) found that metal-poor field stars on the upper RGB had  $[C/Fe]$  ratios that were  $\sim 0.5$  dex lower than those on the main sequence or turn-off. We very clearly see this trend in the pilot

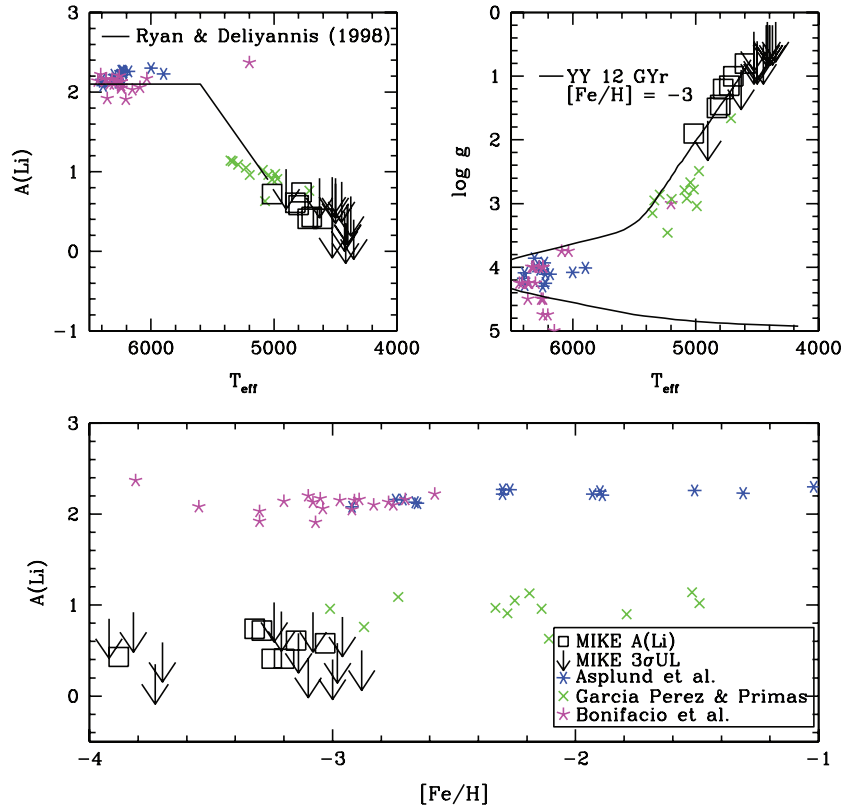


**Figure 10.** MIKE Li abundances (open squares) and upper limits (arrows) plotted against  $[Fe/H]$  along with Li abundances from Asplund et al. (2006), García Pérez & Primas (2006), and Bonifacio et al. (2007) (bottom), and effective temperature with the expected Li dilution curve from Ryan & Deliyannis (1998; top left) overlaid. Effective temperatures and surface gravities are plotted, along with a  $[Fe/H] = -3$ , 12 Gyr Yale-Yonsei isochrone (Green et al. 1984; Kim et al. 2002) for each star plotted in the bottom panel (top right).

(A color version of this figure is available in the online journal.)

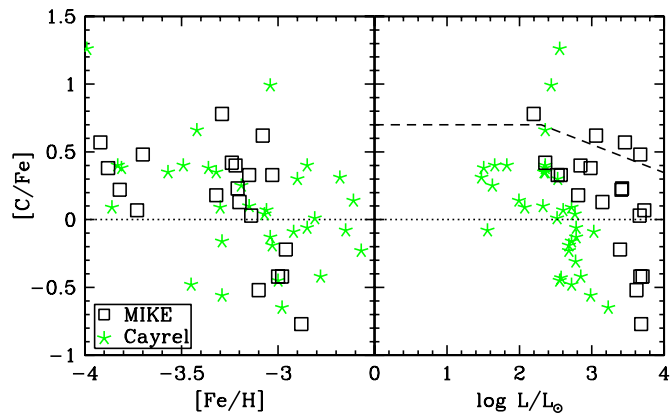


**Figure 11.**  $[C/Fe]$  abundance ratios plotted against  $[Fe/H]$  (left) and luminosity along with the CEMP defining line, which changes over the course of the stellar lifetime (Aoki et al. 2007a; right), along with the calculated Cayrel et al. (2004) C abundances. The  $[C/Fe]$  abundances clearly decline as stars ascend the giant branch.

(A color version of this figure is available in the online journal.)

sample stars, all of which are on the RGB, in Figure 11, where the  $[C/Fe]$  ratio drops by  $\sim 1.2$  dex over one solar luminosity.

Aoki et al. (2007a) provided a new definition for CEMP star status: stars with  $\log(L/L_{\odot}) < \sim 2.3$  and  $[C/Fe] \geq 0.70$  and stars with  $\log(L/L_{\odot}) > \sim 2.3$  and  $[C/Fe] > (3.0 - \log(L/L_{\odot}))$  are considered CEMP stars (see the right panel of Figure 11). This definition takes into account the decrease in the surface C abundances as a function of evolutionary status. For our sample, the definition would indicate that four stars are significantly

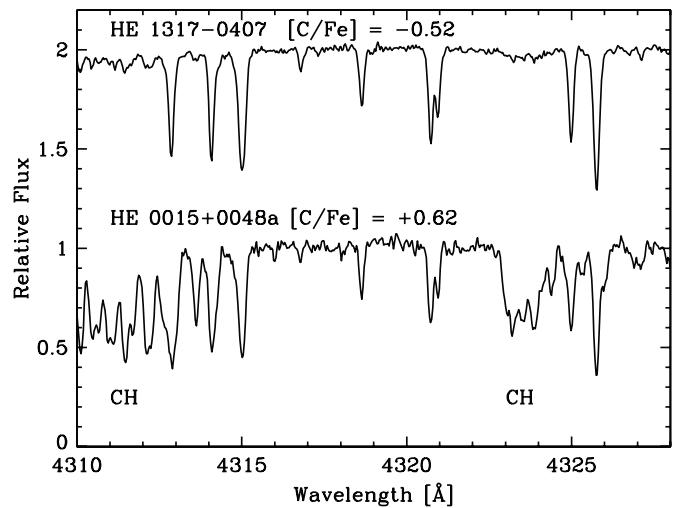


**Figure 12.** HRS spectra of a CEMP star (HE 0015+0048a) and a non-CEMP (HE 1317-0407) star of similar temperatures ( $\sim 4550$  K) and metallicities ( $\sim -3.1$ ).

enhanced in their  $[C/Fe]$  ratios compared to the rest of the sample. This is still true when the effects on the abundances due to the use of different temperature scales are taken into account. In order to study the initial stellar abundances, corrections, up to  $\sim 1$  dex for the highest luminosity stars, should be applied. Thus, if we were to correct for this depletion, one can estimate that the interstellar medium (ISM) from which these stars formed was enriched in C by a factor of  $\sim 10$  or more.

Nevertheless, the large scatter in the [C/Fe] ratios of metal-poor stars indicates a complex production history of C. Additionally, the sizable fraction of metal-poor stars that show enhancement in their [C/Fe] ratio (Frebel et al. 2006; Cohen et al. 2006; Carollo et al. 2011) make it important to study the origin of C in the early universe. For metal-poor stars, the most important production site of C is massive stars that can release CNO elements during the course of stellar evolution through various supernova outbursts (e.g., Fryer et al. 2001; Meynet et al. 2006; Kobayashi et al. 2011).

With these considerations in mind, our C abundances suggest one of the following three scenarios: (1) strong stellar winds from massive stars released C from their atmospheres, enriching only the local ISM; (2) after enrichment from the supernovae of massive stars and/or stellar winds in the early universe, there was only inhomogeneous mixing of the ISM; or (3) the sample stars did not all form from the same molecular cloud or in the same host system. For example, some of the surviving ultra-faint dwarf spheroidal galaxies show an  $\sim 1$  dex spread in their C abundances (Norris et al. 2010a, 2010b). Scenario two does not agree with the small scatter seen in their  $\alpha$ -element ratios. The first and third scenarios, however, are not mutually exclusive. Future modeling of the nucleosynthetic yields of massive Population III stars will facilitate a better understanding of early carbon production. Given the size and metallicity range of the pilot sample, unfortunately nothing can be said about the CEMP frequency, though we will be able to evaluate this using the full CASH sample.

Finally, fine-structure lines of C and O are thought to play a role in the transition from Population III to Population II stars through the cooling of gas clouds of the early universe (Bromm & Loeb 2003). This hypothesis can be tested by comparing the abundances of C and O of metal-poor stars to an abundance transition discriminant as described in Frebel et al. (2007a). Stars with  $[\text{Fe}/\text{H}] < -3.5$  are particularly interesting in this regard; however, all stars of the pilot sample are too C-rich to indicate that fine-structure cooling *did not* play a role.

### 7.2. $\alpha$ -Elements

The  $\alpha$ -elements are created both in core-collapse supernova and through stellar nucleosynthesis in high-mass stars. While the dominant isotope of Ti is not technically an  $\alpha$ -element, it shows an abundance pattern similar to the  $\alpha$ -elements and thus is included here (e.g., Woosley & Weaver 1995). Magnesium and Ca, as well as the other  $\alpha$ -elements, have been shown to be overabundant, compared to the solar system  $[\alpha/\text{Fe}]$  ratio, at low metallicities in field halo stars at the  $\sim 0.4$  dex level (e.g., McWilliam 1997; Cayrel et al. 2004; Frebel 2010). This has been explained by the occurrence of core-collapse supernovae in the early universe, which produce an overabundance of the  $\alpha$ -elements compared to Fe. Later generations of supernovae, specifically Type Ia, produce more Fe, driving down the  $[\alpha/\text{Fe}]$  ratio to that we see today in the Sun and similar young, metal-rich stars. This downturn in the  $[\alpha/\text{Fe}]$  ratio occurs at  $[\text{Fe}/\text{H}] \sim -1.5$ . As our sample does not reach  $[\text{Fe}/\text{H}] > -2.0$ , we do not expect to see this downturn in the  $[\alpha/\text{Fe}]$  abundance ratios.

As seen in other halo stars, the [Mg/Fe] ratio is enhanced relative to the solar ratios in all our sample stars at 0.56 dex. This is also seen in the Cayrel et al. (2004) stars, though there is an offset of  $\sim 0.25$  dex between these two samples, with ours having the larger value. This is due to the differences in the effective temperature scales chosen. The Cayrel et al. (2004) study used (higher) photometric temperatures. To demonstrate

this, we took the Cayrel et al. (2004) equivalent widths for BD  $-18$  5550 and ran them through the Cashcode pipeline. We obtained a temperature different by 150 K, resulting in an offset of 0.5 dex in the surface gravity. In most elemental ratios, these effects cancel, but Mg, especially the triplet, is gravity sensitive, resulting in a  $\sim 0.25$  dex offset in [Mg/Fe] between the two studies.

The [Ca/Fe] ratio is also enhanced in our sample stars relative to the solar ratio at 0.42 dex. The [Ti/Fe] ratio is found to be enhanced relative to the solar ratio in all but two stars, HE 2148–1105a and HE 2302–2145a, with [Ti/Fe] values of  $-0.14$  and  $-0.03$ , respectively; however, both stars show the expected enhancement in [Ca/Fe] (0.17 and 0.31). The [Mg/Fe] values (0.27 and 0.30) in these stars are somewhat lower compared to those in our other stars. The average [Ti/Fe] value for this study is 0.22. The average  $[\alpha/\text{Fe}]$  value is  $\sim 0.4$  dex and thus corresponds well to the average halo  $[\alpha/\text{Fe}]$  values.

### 7.3. Fe-Peak Elements

The [Sc/Fe] ratio for the stars in the sample is generally clustered around the solar abundance ratio. The [Cr/Fe] and [Mn/Fe] abundance ratios for all of our sample stars are found to be deficient relative to the solar abundance by  $-0.23$  and  $-0.49$  dex, respectively. Note that the [Cr/Fe] ratios are based on only the Cr I abundances, as there is a  $\sim 0.35$  dex offset between Cr I and Cr II derived abundances. The [Co/Fe], [Ni/Fe], and [Zn/Fe] ratios in the sample stars are generally enhanced relative to the solar abundance ratios by 0.42, 0.05, and 0.25 dex, respectively.

The Fe-peak elements are created in various late burning stages (see Woosley & Weaver 1995), as well as in supernovae. Our Fe-peak abundance trends follow those of other halo star samples and generally indicate a successive increase of these elements over time (e.g., McWilliam 1997). We will use the Fe-peak elemental abundances of the large CASH sample to put constraints on the nucleosynthesis yields of the progenitor stars. For example, the measured Zn abundances, which we can measure in the HRS spectra, are sensitive to the explosion energy of supernovae (Nomoto et al. 2006; Heger & Woosley 2010).

### 7.4. Neutron-capture Enhanced Stars

The study of neutron-capture elements allows for testing of different sites of nucleosynthesis, beyond proton and  $\alpha$ -capture. See Sneden et al. (2008) for a comprehensive overview of the neutron-capture stellar abundances. Neutron capture occurs mainly in two locations: in the envelopes of highly evolved AGB stars (*s*-process) and in some sort of explosive event, likely a core-collapse supernova (*r*-process). The contributions of each process to the total elemental abundance of the neutron-capture elements in a given star can be determined by evaluating the collective neutron-capture abundance patterns. For example, in the solar system abundances, the *s*-process contributes  $\sim 80\%$  of the Ba abundance, with an  $\sim 20\%$  contribution from the *r*-process, whereas Eu is made almost entirely from the *r*-process (Sneden et al. 2008); however, these ratios may differ in the early universe. Unfortunately, there are not enough neutron-capture elements detectable in the HRS snapshot spectra to determine whether the abundances of neutron-capture elements in a given star have an *s*- or *r*-process origin.

We measured Sr and Ba for all stars in the MIKE sample. We also detected Y and Zr in many of the stars as well, though



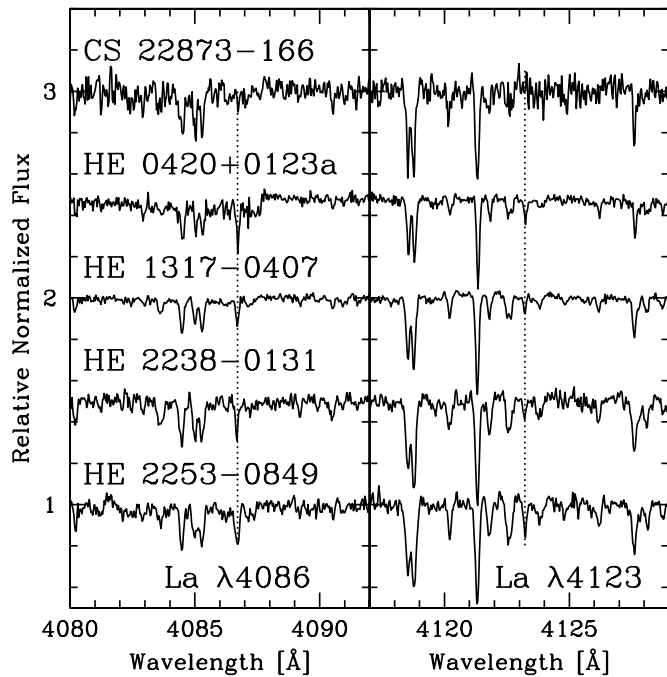


**Figure 13.** La  $\lambda 4086$  and  $\lambda 4123$  line detections in MIKE (black solid line) spectra. Plotted in each panel (dashed line) is the location of the features. For CS 22873–166, only the  $\lambda 4086$  line is a detection.

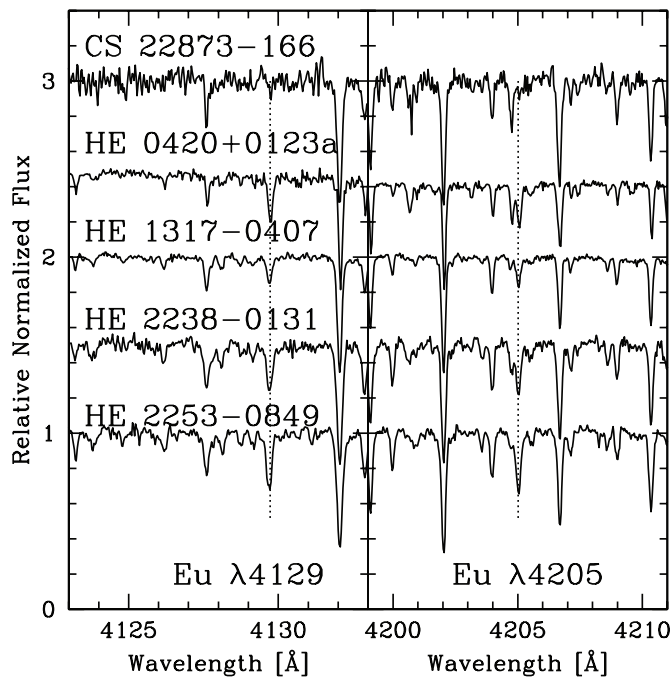


**Figure 14.** Eu  $\lambda 4129$  and  $\lambda 4205$  line detections in MIKE (black solid line) spectra. Plotted in each panel (solid dashed) is the location of the features. For CS 22873–166, only the  $\lambda 4129$  line is a detection.

the S/N near the Y lines often precludes us from measuring it, and the Zr feature is often too weak. We measured La in only four pilot sample stars: HE 2238–0131, HE 0420+0123a, HE 1317–0407, and HE 2253–0840 and in the standard star CS 22873–166. Europium lines have been detected in the high-resolution spectra of the same five stars. In Figures 13 and 14, we show line detections of La and Eu in each star, respectively. The four sample stars are all neutron-capture enhanced, ranging in [Eu/Fe] from 0.02 to 0.79 dex, while CS 22873–166 is depleted

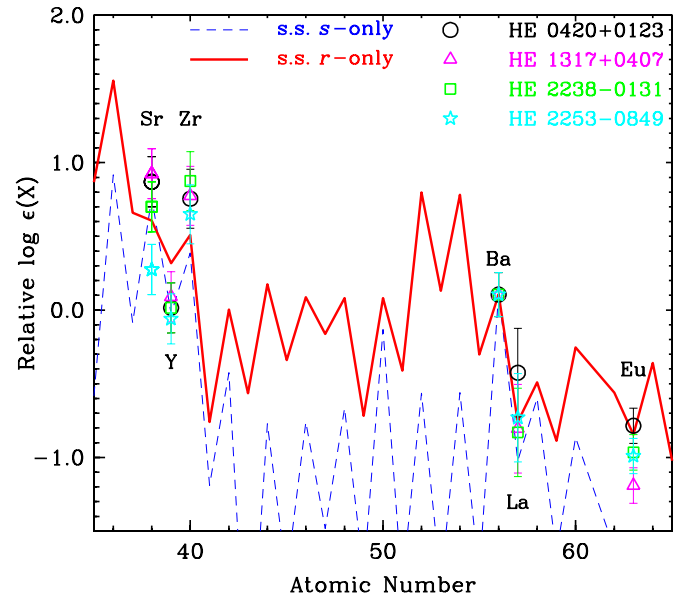


**Figure 15.** Relative  $\log \epsilon(X)$  abundances for all  $r$ -process enhanced stars in the MIKE sample. Abundances are adjusted to the Ba abundance to fit a scaled solar system  $r$ -process curve (red line). The solar system  $s$ -process curve is also plotted (blue dashed line).

(A color version of this figure is available in the online journal.)

in [Eu/Fe] relative to the solar abundance ratio. According to Christlieb et al. (2004), HE 0420+0123a is a mildly  $r$ -process enhanced ( $r$ -I) star due to its [Eu/Fe] ratio (0.79) and Ba/Eu ratio (−0.71).

For each of these neutron-capture enhanced stars, we normalized their  $\log \epsilon(X)$  abundances relative to the Ba abundance and plotted them against a solar system  $r$ -process abundance pattern. We also normalized the solar system  $s$ -process abundance pattern to fit the derived Ba abundance. We found that the  $r$ -process pattern seemed to fit the ratio of La to Eu better than the  $s$ -process pattern, as the Eu abundances would have to be an order of magnitude lower to match the  $s$ -process pattern. Figure 15 shows this analysis. The first neutron-capture peak elements (Sr, Y, Zr) show a  $\sim 0.3$  dex range of abundances, though some are enhanced relative to the  $r$ -process curve. This may indicate two things: (1) the  $r$ -process seems a likely explanation for the Eu abundances, and (2) a nucleosynthetic event besides the same  $r$ -process that formed a portion of the neutron-capture elements in the solar system must be contributing in some of the stars to explain their first neutron-capture peak elemental abundance range.

### 7.5. Stars with [Fe/H] < −3.5

Four stars in the pilot sample have [Fe/H] < −3.5, along with an additional standard star, CS 22891–200, which was found to have a lower [Fe/H] value (−3.92) than that previously published by McWilliam et al. 1995 (−3.49).

All of these extreme EMP (EEMP) stars have enhancements in the  $[\alpha/\text{Fe}]$  ratios, and depletion in some of the Fe-peak abundance ratios, and none are neutron-capture enhanced. We detected the  $\lambda 6707$  Li I line in HE 2302–2154a, which can be expected given that it is the warmest of the EEMP stars at  $T_{\text{eff}} = 4675$  K. Generally, these stars are indistinguishable from the rest of the sample, with the following exception.

It is noteworthy that all five EEMP stars show enhancement in their [C/Fe] abundance ratios. This confirms the trend toward

higher [C/Fe] ratios toward lower values of [Fe/H], noted first by Rossi et al. (2005) and Lucatello et al. (2006). Without consideration for the evolutionary stage of the stars, the average [C/Fe] ratio for the EEMP stars is 0.43, while the rest of the sample has an average [C/Fe] ratio of 0.07 dex. However, given the high luminosity of the EEMP stars, the [C/Fe] ratios have been depleted due to the operation of the CN cycle. Taking this effect into account, two stars are mildly C enriched and two are considered CEMP stars following the definition of Aoki et al. (2007a). The two CEMP stars lack neutron-capture enhancement, which indicates that these stars are CEMP-no stars (Beers & Christlieb 2005), adding to the growing number of these objects at the lowest metallicities.

We did not detect either the La or Eu lines in any of these stars. This is largely due to the fact that it is difficult to detect Eu in EMP stars unless the Eu abundance is significantly enhanced. Given that we do not see strong La enhancement along with the carbon enhancement in the EEMP stars, it is likely that their observed abundance patterns were the result of massive stars, rather than low-mass stars, which produce La in the AGB stage of stellar evolution.

### 7.6. Binary Fraction

For twelve of the pilot sample stars, we derived multiple-epoch measurements of their radial velocity. For three stars, we have additional radial velocity measurements from the solar spectrum-contaminated HET HRS spectra. For the remaining two stars, we do not have multiple measurements. Generally, the radial velocity measurements were taken with a baseline of at least one year and in some cases, three years. The HRS and MIKE radial velocities agree to within  $2.5 \text{ km s}^{-1}$  for those stars. We find one binary candidate in our sample. HE 0015+0048 is the one exception; the time span between measurements is three years and we find a radial velocity variation of  $8.0 \text{ km s}^{-1}$ . Future monitoring of this star will confirm its binarity. This sample is too small to make any definitive statement on the binary fraction of metal-poor stars.

## 8. SUMMARY

We have presented the abundances or upper limits of 20 elements (Li, C, Mg, Al, Si, Ca, Sc, Ti, Cr, Mn, Fe, Co, Ni, Zn, Sr, Y, Zr, Ba, La, and Eu) for 16 new stars and four standard stars derived from high-resolution, high-S/N MIKE spectra via traditional manual analysis methods using the MOOG code. We find that, with the exception of Mg, our abundances match well with those of other halo stars reported in the literature, e.g., Cayrel et al. (2004).

In the pilot sample, we find several distinct chemical groupings of stars, indicating that different enrichment mechanisms may apply for each of these groups, though the exact mechanism is still uncertain. We find four new stars with  $[\text{Fe}/\text{H}] < -3.6$ , where the metallicity distribution function severely drops. We find CS 22891–200 to have a lower [Fe/H] value than reported by McWilliam et al. (1995), bringing the total number of  $[\text{Fe}/\text{H}] < -3.6$  stars to five. All of these stars are enhanced in their [C/Fe] abundance ratios relative to the solar values. We have four CEMP stars in our sample. Two of these are EEMP CEMP-no stars, which confirms the trend of an increasing enhancement in C toward lowest metallicities without invoking the contribution of AGB stars at the lowest metallicities. This may suggest that massive stars released C from their atmospheres and enriched the local ISM and/or that the sample stars did

not all form in the same region. We detected La and Eu in five stars. Of these, four are neutron-capture element enhanced with *r*-process signatures, based upon their [Eu/Fe] ratios, ranging from 0.02 to 0.79; the star with the highest [Eu/Fe] abundance ratio is an *r*-I star. For the remaining stars, we generally find scaled solar system abundance ratios with very small scatter in the abundances. This may indicate the presence of core-collapse supernovae in the early universe. In the pilot sample, we have one star that is a binary candidate. Future monitoring of this star will determine its binarity status.

We presented a calibration of the Cashcode pipeline. We find agreement between the spectroscopic stellar parameters derived from the high-resolution spectra and the snapshot spectra to within  $\Delta T_{\text{eff}} \pm 55 \text{ K}$ ,  $\Delta \log g \pm 0.3 \text{ dex}$ ,  $\Delta[\text{Fe}/\text{H}] \pm 0.15 \text{ dex}$ , and  $\Delta \xi \pm 0.21 \text{ km s}^{-1}$ . These fall within the expected uncertainties associated with snapshot-quality data. We also find that the abundances derived from the HRS spectra using the pipeline are in agreement to within  $1.5\sigma$ . The Cashcode pipeline will be employed for the full  $\sim 500$  star snapshot sample. This sample will be used to determine carbon and neutron-capture enhancement frequencies, to better understand supernova nucleosynthesis and early universe chemical enrichment processes, and find new astrophysically interesting stars that merit further study. One star has already been identified as neutron-capture enhanced in our sample, based on its high Eu abundance and another separate star has also been singled out. The latter star is a CEMP star, with *r*-process and *s*-process elemental abundance enhancements. Both of these will be further analyzed in a later paper as part of this series.

The Hobby-Eberly Telescope (HET) is a joint project of the University of Texas at Austin, the Pennsylvania State University, Stanford University, Ludwig-Maximilians-Universitt Mnchen, and Georg-August-Universitt Gttingen. The HET is named in honor of its principal benefactors, William P. Hobby and Robert E. Eberly. We are grateful to the Hobby-Eberly staff for their assistance in obtaining the data collected for this paper. We thank John Norris and Norbert Christlieb for their valuable contributions to the discovery of the bright metal-poor stars analyzed here. J.K.H. and T.C.B. acknowledge partial support through grants PHY 02-16783 and PHY 08-22648: Physics Frontier Center/Joint Institute for Nuclear Astrophysics (JINA). A.F. acknowledges support of a Clay Fellowship administered by the Smithsonian Astrophysical Observatory. I.U.R. is supported by the Carnegie Institution of Washington through the Carnegie Observatories Fellowship. C.S. is supported through NSF grant AST-0908978.

## REFERENCES

- Alonso, A., Arribas, S., & Martnez-Roger, C. 1999, *A&AS*, **140**, 261  
 Andrievsky, S. M., Spite, M., Korotin, S. A., et al. 2009, *A&A*, **494**, 1083  
 Andrievsky, S. M., Spite, M., Korotin, S. A., et al. 2010, *A&A*, **509**, A88  
 Andrievsky, S. M., Spite, F., Korotin, S. A., et al. 2011, *A&A*, **530**, A105  
 Aoki, W., Beers, T. C., Christlieb, N., et al. 2007a, *ApJ*, **655**, 492  
 Aoki, W., Honda, S., Beers, T. C., et al. 2007b, *ApJ*, **660**, 747  
 Asplund, M. 2005, *ARA&A*, **43**, 481  
 Asplund, M., Lambert, D. L., Nissen, P. E., Primas, F., & Smith, V. V. 2006, *ApJ*, **644**, 229  
 Barklem, P. S., Christlieb, N., Beers, T. C., et al. 2005, *A&A*, **439**, 129  
 Baumueler, D., & Gehren, T. 1997, *A&A*, **325**, 1088  
 Beers, T. C., & Christlieb, N. 2005, *ARA&A*, **43**, 531  
 Beers, T. C., Preston, G. W., & Shectman, S. A. 1985, *AJ*, **90**, 2089  
 Beers, T. C., Preston, G. W., & Shectman, S. A. 1992, *AJ*, **103**, 1987  
 Bergemann, M., & Gehren, T. 2008, *A&A*, **492**, 823

- Bernstein, R., Shectman, S. A., Gunnels, S. M., Mochnacki, S., & Athey, A. E. 2003, *Proc. SPIE*, **4841**, 1694
- Bohlin, R. C., Jenkins, E. B., Spitzer, L., et al. 1983, *ApJS*, **51**, 277
- Bonifacio, P., Molaro, P., Sivarani, T., et al. 2007, *A&A*, **462**, 851
- Bromm, V., Coppi, P. S., & Larson, R. B. 1999, *ApJ*, **527**, L5
- Bromm, V., & Loeb, A. 2003, *Nature*, **425**, 812
- Cameron, A. G. W., & Fowler, W. A. 1971, *ApJ*, **164**, 111
- Carney, B. W., Laird, J. B., Latham, D. W., & Aguilar, L. A. 1996, *AJ*, **112**, 668
- Carollo, D., Beers, T. C., Bovy, J., et al. 2011, arXiv:1103.3067
- Cassisi, S., Castellani, M., Caputo, F., & Castellani, V. 2004, *A&A*, **426**, 641
- Castelli, F., & Kurucz, R. L. 2003, in Proc. 210th IAU Symp., Modelling of Stellar Atmospheres, ed. N. Piskunov, W. W. Weiss, & D. F. Gray (San Francisco, CA: ASP), A20
- Cayrel, R., Depagne, E., Spite, M., et al. 2004, *A&A*, **416**, 1117
- Christlieb, N., Beers, T. C., Barklem, P. S., et al. 2004, *A&A*, **428**, 1027
- Christlieb, N., Gustafsson, B., Korn, A. J., et al. 2004, *ApJ*, **603**, 708
- Christlieb, N., Wisotzki, L., Reimers, D., et al. 2001, *A&A*, **366**, 898
- Cohen, J. G., McWilliam, A., Shectman, S., et al. 2006, *AJ*, **132**, 137
- Frebel, A. 2010, *Astron. Nachr.*, **331**, 474
- Frebel, A., Aoki, W., Christlieb, N., et al. 2005, *Nature*, **434**, 871
- Frebel, A., Christlieb, N., Norris, J. E., et al. 2006, *ApJ*, **652**, 1585
- Frebel, A., Johnson, J. L., & Bromm, V. 2007a, *MNRAS*, **380**, L40
- Frebel, A., Norris, J. E., Aoki, W., et al. 2007b, *ApJ*, **658**, 534
- Fryer, C. L., Woosley, S. E., & Heger, A. 2001, *ApJ*, **550**, 372
- Fulbright, J. P. 2000, *AJ*, **120**, 1841
- García Pérez, A. E., & Primas, F. 2006, *A&A*, **447**, 299
- Gratton, R. G., & Sneden, C. 1988, *A&A*, **204**, 193
- Gratton, R. G., Sneden, C., Carretta, E., & Bragaglia, A. 2000, *A&A*, **354**, 169
- Green, E. M., Demarque, P., & King, C. R. 1984, *BAAS*, **16**, 997
- Heger, A., & Woosley, S. E. 2010, *ApJ*, **724**, 341
- Keeping, E. S. 1962, *Introduction to Statistical Inference* (Princeton, NJ: Van Nostrand)
- Kim, Y.-C., Demarque, P., Yi, S. K., & Alexander, D. R. 2002, *ApJS*, **143**, 499
- Kobayashi, C., Tominaga, N., & Nomoto, K. 2011, *ApJ*, **730**, L14
- Kurucz, R. L. 1993, *Kurucz CD-ROM 13, ATLAS9 Stellar Atmosphere Programs and 2 km/s Grid* (Cambridge, MA: SAO)
- Li, H. N., Christlieb, N., Schörck, T., et al. 2010, *A&A*, **521**, 10
- Lucatello, S., Beers, T. C., Christlieb, N., et al. 2006, *ApJ*, **652**, L37
- McWilliam, A. 1997, *ARA&A*, **35**, 503
- McWilliam, A., Preston, G. W., Sneden, C., & Searle, L. 1995, *AJ*, **109**, 2757
- Meléndez, J., Casagrande, L., Ramírez, I., Asplund, M., & Schuster, W. J. 2010, *A&A*, **515**, 3
- Meynet, G., Ekström, S., & Maeder, A. 2006, *A&A*, **447**, 623
- Nomoto, K., Tominaga, N., Umeda, H., Kobayashi, C., & Maeda, K. 2006, *Nucl. Phys. A*, **777**, 424
- Norris, J. E., Christlieb, N., Korn, A. J., et al. 2007, *ApJ*, **670**, 774
- Norris, J. E., Gilmore, G., Wyse, R. F. G., Yong, D., & Frebel, A. 2010a, *ApJ*, **722**, L104
- Norris, J. E., Wyse, R. F. G., Gilmore, G., et al. 2010b, *ApJ*, **723**, 1632
- Piskunov, N. E., & Valenti, J. A. 2002, *A&A*, **385**, 1095
- Ramírez, I., & Meléndez, J. 2004, *ApJ*, **609**, 417
- Roederer, I. U., Frebel, A., Shetrone, M. D., et al. 2008, *ApJ*, **679**, 1549
- Roederer, I. U., Sneden, C., Thompson, I. B., Preston, G. W., & Shectman, S. A. 2010, *ApJ*, **711**, 573
- Rossi, S., Beers, T. C., Sneden, C., et al. 2005, *AJ*, **130**, 2804
- Ryan, S. G., Beers, T. C., Deliyannis, C. P., & Thorburn, J. A. 1996, *ApJ*, **458**, 543
- Ryan, S. G., & Deliyannis, C. P. 1998, *ApJ*, **500**, 398
- Ryan, S. G., & Norris, J. E. 1991, *AJ*, **101**, 1835
- Schlegel, D. J., Finkbeiner, D. P., & Davis, M. 1998, *ApJ*, **500**, 525
- Schörck, T., Christlieb, N., Cohen, J. G., et al. 2009, *A&A*, **507**, 817
- Shetrone, M., Cornell, M. E., Fowler, J. R., et al. 2007, *PASP*, **119**, 556
- Sneden, C., Cowan, J. J., & Gallino, R. 2008, *ARA&A*, **46**, 241
- Sneden, C. A. 1973, PhD thesis, Univ. Texas at Austin
- Sobeck, J. S., Kraft, R. P., Sneden, C., et al. 2011, *AJ*, **141**, 175
- Spite, F., & Spite, M. 1982, *A&A*, **115**, 357
- Tull, R. G. 1998, *Proc. SPIE*, **3355**, 387
- Woosley, S. E., & Weaver, T. A. 1995, *ApJS*, **101**, 181
- Yanny, B., Rockosi, C., Newberg, H. J., et al. 2009, *AJ*, **137**, 4377
- York, D. G., Adelman, J., Anderson, J. E., Jr., et al. 2000, *AJ*, **120**, 1579